Ph. D. DISSERTATION

HIGHLY EFFICIENT QUANTUM DOT LIGHT-EMITTING DIODES BASED ON THE OPTIMIZATION OF QUANTUM DOT STRUCTURE AND DEVICE ARCHITECTURE

양자점 구조 및 소자 최적화를 통한 고효율
양자점 발광 다이오드

BY

MYEONGJIN PARK

FEBRUARY 2016

DEPARTMENT OF
ELECTRICAL AND COMPUTUER ENGINEERING
COLLEGE OF ENGINEERING
SEOUL NATIONAL UNIVERSITY

HIGHLY EFFICIENT QUANTUM DOT LIGHT-EMITTING DIODES BASED ON THE OPTIMIZATION OF QUANTUM DOT STRUCTURE AND DEVICE ARCHITECTURE

양자점 구조 및 소자 최적화를 통한 고효율 양자점 발광 다이오드

지도교수 이 창 희

이 논문을 공학박사 학위논문으로 제출함

2016 년 2 월

서울대학교 대학원

전기컴퓨터 공학부

박 명 진

박명진의 공학박사 학위논문을 인준함

2016 년 2 월

위 원 장 : _____ (인)
부위원장 : _____ (인)
위 원 : _____ (인)
위 원 : _____ (인)
위 원 : _____ (인)

Abstract

HIGHLY EFFICIENT QUANTUM DOT LIGHT-EMITTING DIODES BASED ON THE OPTIMIZATION OF QUANTUM DOT STRUCTURE AND DEVICE ARCHITECTURE

MYEONGJIN PARK
DEPARTMENT OF ELECTRICAL AND COMPUTER ENGINEERING
COLLEGE OF ENGINEERING
SEOUL NATIONAL UNIVERSITY

Semiconductor nanocrystals or colloidal quantum dots have many advantages because their superb optical and electrical properties can be tuned via shape- and size-control. To utilize these properties, substantial research has been devoted to enable semiconductor nanoparticles to be applied in next-generation optoelectronics

(e.g., light-emitting diodes (LEDs), solar cells, and photo catalysts). For many years, the device fabrication processes and performances of quantum dot light-emitting diodes (QLEDs) have undergone substantial development because of efforts addressing material synthesis, electrophysical analysis and device design. Thus, the tailoring of the structure of semiconductor nanocrystals to control optical or electrical properties and their applications in optoelectronic devices must be discussed.

In this thesis, high-performance colloidal QLEDs were studied from the perspective of device mechanism and device structure engineering. We developed and demonstrated highly efficient red, green, and blue (RGB) QLEDs with improved group II-VI QDs and environmentally benign Cd-free QDs.

First, we investigated the influence of the shell thickness of group II-VI type-I heterostructure QDs on the QLED performance. We found that thick-shell QDs exhibited reduced Auger-type decay rates and suppressed energy transfer (ET) within QD films. In addition, we characterized the device performance and found high efficiency (peak EQE ~ 7.4 %) and record brightness (105,870 cd/m2). The operation stability of the devices is presented along with the improved device performance. Our suggestions for QLED design offer simple results and approaches but propose novel structural designs of core/shell heterostructure QDs to allow engineering of the optical properties of QD solids and the performances of corresponding devices; in addition, they provide rational guidelines for the practical use of QLEDs in high-power light sources.

To improve the electron transport layers (ETLs), we demonstrate that the efficiency of inverted QLEDs is enhanced by using a double electron transport layer (ETL) consisting of ZnO nanoparticles and 1,3,5-tris(N-phenylbenzimidizol-2-yl)benzene (TPBI) as an organic electron transport material. TPBI, as a soluble

organic electron transport material, fills the voids in the ZnO nanoparticle film and thereby reduces the leakage current path. As a result, the efficiency of blue QLEDs was considerably increased, reaching a maximum EQE of 3.4 %.

For highly efficient InP QLEDs, the inverted device structure with a ZnO electron transporting layer (ETL) was adopted because of its numerous advantages in process and integration. However, the large difference in the conduction band (CB) between InP QDs and ZnO impedes efficient electron injection from ZnO to InP QDs. To solve the injection issue, a solution-processable poly[(9,9-bis(3′ -(N,N-dimethylamino)propyl)-2,7-fluorene)-alt-2,7-(9,9-ioctylfluorene (PFN) layer was selected as an interfacial dipole layer. Because of differences in the solubility of ZnO, PFN, and QDs, stacking the three different layers substantially improved device performance in terms of maximum external quantum efficiency (EQE) of 3.46 % and a maximum luminance of 3900 cd/m2. In our forthcoming research, we believe that an in-depth investigation of nonradiative multicarrier decay during device operation and minute engineering of the core@shell heterostructure to minimize such processes will guide us one step further toward producing high–performance InP QLEDs.

This thesis demonstrates a novel approach to increase the efficiency and carrier injection of inverted QLEDs. Furthermore, the physical properties of QDs were systematically studied to establish a method to maximize device performance. In addition, the novel InP QLED structure may be applied to a variety of optoelectronic devices, such as thin-film solar cells, LEDs and transistors.

Keywords: Colloidal Quantum Dot, Light-Emitting Diodes, Inverted Structures, Energy Transfer, Cadmium Free, Conjugated Polyelectrolyte

Student Number: 2010-20799

Contents

List of Figures

List of Tables

Chapter 1

Introduction

1.1 Colloidal Quantum Dot Light-Emitting Diodes

Colloidal quantum dot light-emitting diodes (QLEDs) have attracted significant attention as a promising future display technology for over 20 years. The advantages of colloidal quantum dots (QDs) have prompted widespread efforts to develop QD-based technologies for displays [1-4], lighting, bio-imaging [5, 6], light-harvesting [7], and sensing applications [8]. The major benefits of QDs are high photoluminescence (PL) quantum yields (Qys), broad absorption area, narrow emission spectra, high colloidal and electrical stability, and processability. When QDs are utilized, particularly as luminescent materials in light-emitting diodes (LEDs), the resulting displays are believed to outperform their competitors by taking advantage of the superior color purity, quantum efficiency and stability of semiconductor nanocrystals [9, 10]. In addition to the performance, the inherent solubility imparted by surface-stabilizing ligands is another benefit for the

affordable production of large-area, flexible displays using solution-based printing methods [2, 3, 11].

Currently, organic light-emitting diodes (OLEDs) constitute the premier display technology because of their various advantages. However, the electroluminescence (EL) emission spectra of OLEDs are much broader than those of QLEDs. The bandwidth of EL devices is critical in determining color purity and color ranges in the color gamut. In the case of Cd-based QLEDs, the usual full width at half maximum (FWHM) of QLEDs is less than 30 nm; that is, QLEDs exhibit considerable color purity in each color. Figure 1.1a clearly shows that the EL spectra of red, green, and blue (RGB) QLEDs and OLEDs are quite different. Among the spectra, OLEDs EL spectra were collected from well-known phosphorescent devices with bis(1-phenylisoquinolinato) iridium(III) (acetylacetonate) ($(piq)_2Ir(acac)$) as the red dopant and fac-tris(2-phenylpyridine) iridium(III) ($Ir(ppy)_3$) as the green dopant in 4,4'-N,N'-dicarbazole-biphenyl (CBP) layers and iridium(III) bis(4,6-(difluorophenyl) pyridinato-N,C2') picolinate (Firpic) as the blue dopant in the N,N'-dicarbazolyl-3,5-benzene (mCP) layer. Figure 1.1b clearly shows the advantages of QLEDs in wide color ranges. Through the advancement of QD synthesis technologies, the color purity of QDs has continuously improved. QLEDs utilizing very pure color QDs can achieve excellent color gamut, better than those previously reported. Because of these outstanding optical properties, QDs are regarded as the most promising next-generation lumophors in the display and lighting industries.

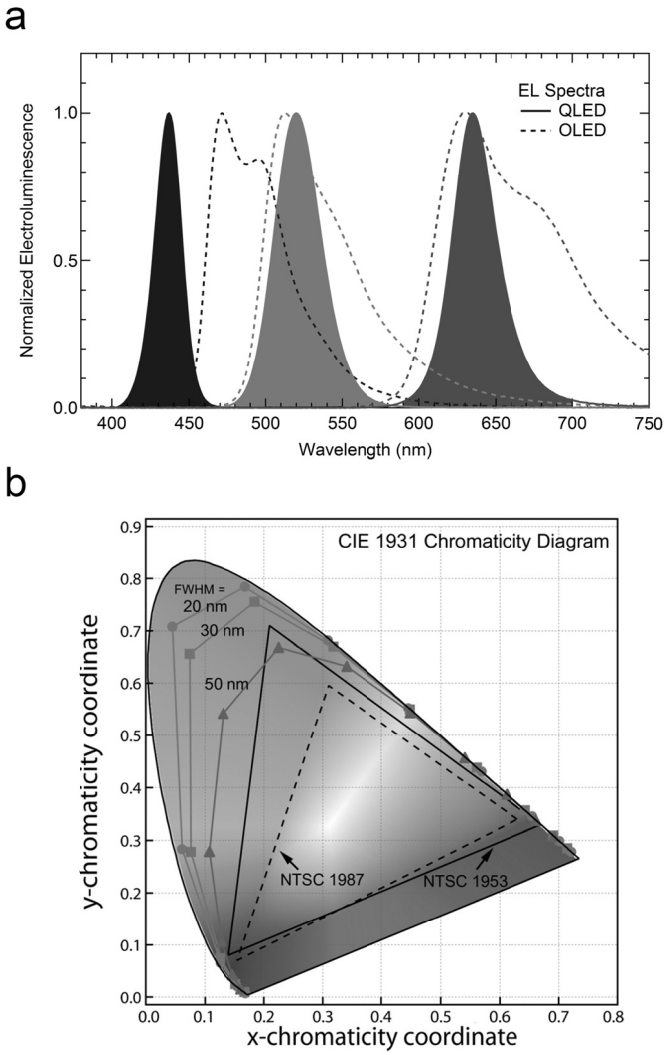

Figure 1.1 (a) Comparison of red, green and blue EL spectra with (dashed lines) OLEDs and (solid lines) QLEDs, (b) The CIE (Commission Internationale de l'Eclairage) 1931 chromaticity diagram of hypothetical QDs emitting 420, 450, 470, 490, 510, 530, 550, 570, 590, 610, 630 and 650 nm (from the left) with 20 nm (red dot), 30 nm (green square) or 50 nm (blue triangle) of FWHM. NTSC 1987 (solid line) and 1953 (dashed line) color gamut are also illustrated. The emission spectra of QDs are assumed as Gaussian shape. [12]

The history of QLEDs is presented in Figure 1.2. The first QLED was reported by V.L Colin *et al*. [2] The introduced devices had a simple layer structure, which was composed of indium tin oxide (ITO)//conjugated polymer (poly(*p*-paraphenylene vinylene) (PPV)) as a hole transporting layer (HTL)//CdSe QDs//Mg as a low work function cathode. They showed clear EL spectra stemming from CdSe QDs but low efficiency and brightness (i.e., EQE: 0.001 ~ 0.01 %, brightness: ~100 cd/m^2). Colin *et al.* used only core QDs in QLEDs; subsequently, improved materials were developed that were capable of 0.22 % EQE and 10-fold higher brightness. [13]; however, low PL QY and low stability issues remained, thus accounting for the imbalanced charge carrier injection and the recombination of excitons. To solve these issues, S. Coe *et al.* first reported the use of a HTL and electron transporting layer (ETL) to achieve balanced charge carrier injection similar to that in the conventional OLED structure. [3] They adopted the ITO//TPD//CdSe QDs//Alq3/Mg structure, with N, N′-diphenyl-N,N′-bis(3-methyl phenyl)-(1,1′-biphenyl)-4,4′-diamine (TPD) as the HTL and tris-(8-hydroxyquinoline)aluminum (Alq3) as the ETL (Figure 1.2). To improve the performance, this group later suggested a revised device structure (ITO//HTL//CdSe QDs//electron blocking layer (EBL)//Mg) to facilitate charge injection or energy transfer (ET) from adjacent organic layers into QDs. Without an EBL (3,4,5-triphenyl-4H-1,2,4-triazole [TAZ], 10 nm), the device spectra included a parasitic peak from the adjacent organic layers. To reduce the emission peak from HTL, they inserted TAZ and improved the device performance (i.e., EQE: 0.52 %, luminous efficiency: 1.6 cd/A). [3]

Since the multilayered QLEDs structure was developed, the research on QLEDs has progressed rapidly. In the past 10 years, many groups have reported substantially improved performance over that in previous reports. In fact, these recent reports already satisfy the criteria for commercial full-color displays; that is,

the device performance has reached 100 ~ 500 cd/m^2 for mobile displays and over 1000 cd/m^2 for TVs with color reproduction. In addition, to solve the issues associated with the large energy barrier between QDs (the valence band [VB] edge is ~7 eV) and organic hole transporting material (the highest occupied molecular orbital (HOMO) energy level is 5–6 eV), J. Kwak *et al.* have suggested a new device architecture, i.e., an inverted structure. [9] Since then, many groups have developed QLEDs using these two typical structures. Although the inverted structure has been suggested to solve the hole injection problem in the standard structure, both QLED structures have been reported to exhibit high efficiency. In particular, the EQEs of RG QLEDs are rapidly approaching 20 %, [14, 15] which is a theoretical limit, with 20 % extraction efficiency assumed. [16] Although blue QLEDs are still far from successful commercialization, the drastic increase in device efficiency indicates their promise for future use in practical devices.

In addition to Cd-based QLEDs, Cd-free QLEDs has been developed in recent years. The EQEs of Cd-free QLEDs are still below those of Cd-based QLEDs. Because many groups have steadily continued their efforts to improve the efficiency of Cd-free QLEDs, these QLEDs are expected to reach the level of Cd-based QLEDs.

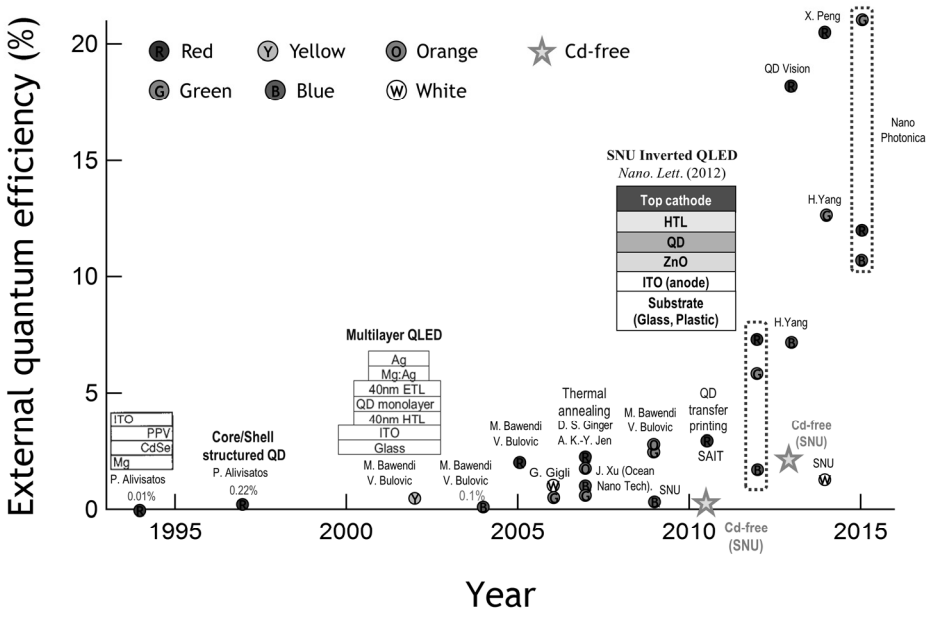

Figure 1.2 Progress in external quantum efficiency (EQE) of QLEDs. The EQE values were categorized into seven types (Red (770–600 nm), Orange (600–570 nm), Green (570–500 nm), Blue (500–430 nm), White and Cd-free. [2-4, 9, 10, 13-15, 17-30]

Recently, an efficient active matrix display device using QDs on a low-temperature polycrystalline silicon (LTPS) thin-film transistor (TFT) backplane has been developed by NanoPhotonica Inc. [15] A cross-linkable hole transporting material (poly[9,9-dioctylfluorenyl-2,7-diyl)-co-(4,4'-(*N*-(4-sec-butylphenyl))diphenylamine)], TFB) and ZnO_2 as an ETL was adopted to fabricate the device with a solution–based process. A display device with a size of 4.3 in with a 480 × 800 pixel array operated with an active matrix drive was demonstrated, as shown in Figure 1.3; this accomplishment indicates that practical QLED displays will be realized soon.

Figure 1.3 Display image of 4.3-inch red and green QLED using a LTPS TFT backplane with a 480 × 800 pixel array for the active matrix drive. [15] (The image is taken from ref. [15])

1.2 Key Issues for Improving the Performances of QLEDs

The rapidly developing nanotechnologies involved in QLEDs have been investigated to satisfy scientific interest regarding their unique optoelectronic device properties and to take advantage of their highly efficient applications. Although chemical development, which is related to low PL QY and low stability issues, is quite important, the design of the device architecture is more critical to achieving successful commercial application. These device structure issues are closely connected to the imbalanced charge carrier injection and recombination of excitons.

Several studies on inverted structure have been reported in the OLED field [31, 32]. For bottom emission inverted OLEDs, the bottom cathode must be optically transparent while also facilitating electron injection. However, ITO, which is commonly used as a transparent electrode, is not an appropriate bottom electrode because of its poor electron injection. A large energy offset exists between ITO (the work function of ITO is approximately 4.7 eV) and the lowest unoccupied molecular orbital (LUMO) energy levels of typical organic electron transporting materials (approximately 2 ~ 3 eV). To reduce this offset, we utilized an n-type metal oxide material as an ETL. The electron affinity of both the n-type metal oxides, such as ZnO and SnO_2, and QDs are approximately 4 ~ 4.5 eV; [33, 34] thus, the electron injection barrier from ITO is reduced to 0.2 ~ 0.7 eV. Therefore, QLEDs with a metal oxide ETL are more advantageous than OLEDs with an inverted structure for use with, transparent ITO electrodes without further bottom cathode engineering. In addition, the inverted QLED allows the choice of various hole transporting materials that facilitate hole injection into the QDs, regardless of the deposition process. From a process viewpoint, we can easily deposit solution-based QDs on the top of the metal oxide layer without damaging the underlying film because the metal oxide

layer becomes resistant after thermal annealing. Additionally, various organic hole transporting materials that facilitate hole injection into QDs can be selected and deposited onto a QD layer, as we have reported previously. [9] Therefore, QLEDs adopting metal oxides as the carrier transport layer can exhibit outstanding performance in terms of efficiency, brightness, and stability. It is also notable that QLEDs with metal oxides have extremely low turn-on voltages that can be as low as the voltage equivalent to the band gap energy of QDs. [9, 33, 34] Typically, a large hole injection barrier (~ 1 eV) exists between the HOMO energy levels of typical organic hole transport materials and the VB energy levels of Cd-based QDs. This large hole injection barrier disrupts the hole injection from the organic hole transport layer (HTL) into QDs, resulting in poor device performance characteristics, such as high turn-on and driving voltages and/or light emission from the organic layers and surface states. Despite the large energy barrier, it is interesting that QLEDs are turned on at the voltage corresponding to the QDs' band gap when metal oxides are adopted in the ETL.

QLEDs hold promise for the realization of color-saturated spectra over a variety of wavelengths, ranging from visible to near infrared (IR), based on low-cost solution-processing methods. [2] The advances in the understanding of device physics have prompted developments in device performance and have resulted in QLEDs with near-unity peak internal efficiency. [9, 10, 35] Despite recent rapid progress, daunting issues remain to be solved. The drastic efficiency roll-off behaviors and severe device instabilities under operation are specific problems that limit the use of QLEDs in lighting and lasing applications.

Despite the drastic improvement in device performance and positive outlook, the commercialization of QLEDs will inevitably be limited by the social restrictions of environmental protection and human safety. Most research on QLEDs has utilized

Cd-based QDs because of their high quantum efficiency and well-established synthetic processes. Unfortunately, Cd is highly detrimental to the environment; the bioaccumulation of Cd causes irreversible damage to human organs (i.e., liver and kidney), bone, and muscles and even fatal disease. To prepare for the probable risks posed by Cd-based QDs to humans and the environment, Cd-free nanocrystal phosphors, such as chalcopyrites (i.e., $CuInSe_2$ or $CuInS_2$), [36-38] doped nanocrystals, [39-42] and InP QDs, [26, 43-46] have been suggested for LEDs . In the visible and near IR region, such Cd-free nanocrystals have exhibited controllable emission spectra and high fluorescence quantum efficiency reaching ~ 70 %, comparable to that of Cd-based QDs. However, the spectral bandwidths of chalcopyrites and doped nanocrystals are far inferior (~ 100 nm) to those of the II-VI or III-V QDs (30 ~ 60 nm); as a result, their utilization has been restricted to white LEDs [47] or biomarkers [48] demanding wide emission bands or near IR emission. Consequently, InP QDs have been regarded as peerless alternatives to environmentally benign and efficient phosphors with high color purity for realizing full-color QD displays.

1.3 Outline of Thesis

This thesis consists of six chapters, including the Introduction and Conclusion. As an introduction, Chapter 1 describes the previous research on colloidal QLEDs and the key issues for improving QLED performance. In Chapter 2, the methods used to prepare ZnO nanoparticles; the highly luminescent red, Cd-free green and blue heterostructured QDs; and the organic materials used in this thesis are described in detail. In addition, the fabrication and characterization methods for the QLED devices are summarized in this chapter, and the chemical structures of the organic materials used in this thesis are depicted. In Chapter 3, the influence of the shell thickness of type-I heterostructured QDs on QLED performance is investigated based on red core/shell heterostructured QDs. We studied a series of CdSe/$Zn_{1-x}Cd_xS$ core/shell type-I QDs with different shell thicknesses. Through a systematic study of QLEDs and spectroscopic analysis of QD films in device architectures, we observed that thick-shell QDs exhibited reduced Auger-type decay rates and suppressed ET within QD solids. The photophysical changes are responsible for the alleviated efficiency roll-off and improved stability in QLEDs. The findings are highlighted in the device characteristics: high device efficiency and record-high brightness along with improved device stability. In Chapter 4, we identify the effect of the double ETL used in inverted blue QLEDs, which could lead to important research in terms of the structural design of devices to further improve blue QLEDs. Environmentally benign, highly efficient, and bright InP@ZnSeS QLEDs based on the advanced synthetic method for InP QDs and tailored device structures are systematically characterized in Chapter 5. To identify the effect of the conjugated polyelectrolyte layer in InP QLEDs, we suggest important directions in terms of the structural design of devices and the core@shell formulation of QDs for further

improvements of InP QLEDs. For efficient device structure, we revealed that a thick ZnSeS heterostructured shell is important to increase the EQEs of QLEDs by protecting the electrically generated excitons from surface states. Finally, in Chapter 6, we summarize our work and present concluding remarks.

Chapter 2

Experimental Methods

2.1 Materials

2.1.1 Preparation of ZnO Nanoparticles

ZnO nanoparticles were synthesized modifying the method reported by Pacholski *et al.* [49] 2 g of $Zn(ac)_2 \cdot 2H_2O$ and 80 mL of methanol were first placed in a 3-neck round bottom flask and heated to 60 °C. At 60 °C, a 65 mL KOH solution containing 1.51 g of KOH was added dropwise into the $Zn(ac)_2 \cdot 2H_2O$ solution under strong agitation. The reaction mixture was kept at 60 °C for 2 hr 30 min to yield a milky solution containing ZnO nanoparticles. The ZnO nanoparticles were then isolated by centrifugation at 4000 rpm followed by repetitive washing using methanol. Finally, the product was centrifuged again and re-dispersed in 5 mL of butanol.

2.1.2 Synthesis of Red-color Emitting CdSe/$Zn_{1-X}Cd_XS$ Core/shell Heterostructured Quantum Dots

Chemicals : Cadmium oxide (CdO, 99.9%), zinc oxide (99.9%), selenium (200 mesh, 99.999%), 1-dodecanethiol (DDT, 98%), tri-*n*-octylphosphine (TOP, 90%), myristic acid (MA, 90%) were purchased from Alfa Aesar. Sulfur (99.9%), oleic acid (OA, technical grade) and 1-octadecene (ODE, 90%) were obtained from Sigma Aldrich. General organic solvents were acquired from Daejung (Korea). All chemicals were used as received without further purification.

Synthesis of CdSe/$Zn_{1-X}Cd_XS$ QDs : QD synthesis was preceded with the Schlenk line technique under inert conditions. The cationic precursors (0.5 M cadmium oleate ($Cd(OA)_2$) and 0.5 M zinc oleate ($Zn(OA)_2$)) were prepared by dissolving the 100 mmol of CdO and ZnO in mixed solvent of 100 ml of OA and 100 ml of ODE (total volume 200 ml) under N_2 at 300 °C for 1hr. The anionic precursors (2 M TOPSe and 2 M TOPS) were made by dissolving 20 mmol of selenium and sulfur in 10 ml of TOPSe under N_2 at 100 °C for 1hr. For CdSe/$Zn_{1-X}Cd_XS$ (r = 2.0 nm, R = 4.5 nm), 1 mmol of CdO, 3 mmol of MA and 15 ml of ODE were loaded in 3 neck flask and heated up to 300 ^oC under the inert conditions to form $Cd(MA)_2$ complex. After reactants were turned to be optically clear, 0.25 ml of 2 M TOPSe was rapidly injected into the reaction flask to form CdSe core. After 3 min of reaction, 3 ml of 0.5 M $Zn(OA)_2$ precursor and 1 mmol of DDT were added drop wisely within 1 min. The reaction was preceded for 30 min to yield $Zn_{0.4}Cd_{0.6}S$ inner shell. 2 ml of 0.5 M $Cd(OA)_2$, 4 ml of 0.5 M $Zn(OA)_2$ and 1.5 ml of 2 M TOPS were added into the reaction flask within 1 min for $Zn_{0.5}Cd_{0.5}S$ shelling and the reaction was proceeded for 10 min. The repeated precursor injection yielded the successive growth of $Zn_{0.5}Cd_{0.5}S$ outer shell growth. Synthesized QDs were purified 10 times by the

precipitation/redispersion (ethanol/toluene) method. Final products were dispersed in hexane at a concentration of 20 mg/ml.

2.1.3 Synthesis of Cd-free Green Color Emitting InP/ZnSeS Core/shell Heterostructured Quantum Dots

Modified synthetic procedure by Lim et al. was adopted for the synthesis of InP@ZnSeS QDs. [26] Briefly, 0.1mmol of $InCl_3$ in 1mL of tetrahydrofuran, 2mL of zincoleate ($Zn(OA)_2$, 30 mmol of zinc acetate reacted with 19 mL of oleic acid (OA) under vacuum and diluted with 41 mL of 1-octadecene (ODE)), and 8mL of ODE were loaded in a 100 mL flask with a condenser and degassed for 30 min to remove water and oxygen species. After backfilling the reactor with N_2, temperature was increased to 280 °C and a mixture of 0.1 mmol of $P(TMS)_3$ and 0.4 mmol of STBP (0.4 mmol of sulfur dissolved in 0.5 mL of TBP and 0.5 mL of ODE) was rapidly injected into the reactor. After 20 s, 0.2 mL of SeTOP (0.2 mmol of Se dissolved in 0.5 mL of n-trioctylphosphine and 0.5 mL of ODE) was slowly added for 20 s and reacted at 280 °C for 10 min. Next, 4 mL of $Zn(OA)_2$ and 1.8 mL of 1-dodecanethiol were added and reacted for 90 min at 300 °C. Finally, 6 mL of $Zn(OA)_2$ and 0.72 mL of 1-dodecanethiol were added, and the mixture was reacted for 120 min (for InP@ZnSeS QDs with 1.1 nm shell thickness, this step was omitted). After the reaction was terminated, the mixture was cooled to room temperature to terminate the reaction. For the purification of QDs, a precipitation/redispersion method was employed; the crude solution was precipitated with an excess amount of acetone and redispersed with toluene. After repeated purification processes (typically 4 times), the precipitated QDs were dried under N_2 flow for 5 min and dispersed in hexane (around 50 mg mL^{-1}).

2.1.4 Synthesis of Blue-color Emitting $Cd_{1-x}Zn_xS$@ZnS Quantum Dots

As a synthetic procedure, 1 mM of CdO, 10 mM of $Zn(acet)_2$, 7 mM of OA were placed in a 100 mL round flask. The mixture was heated to 150 °C, degassed under 100 mTorr pressure for 20 minutes, filled with N_2 gas, added with 15 ml of 1-ODE and further heated to 300 °C to form a clear solution of $Cd(OA)_2$ and $Zn(OA)_2$. At this temperature, 2 mM of S powder dissolved in 3 mL of 1-ODE were quickly injected into the reaction flask. After the first injection of S precursors, the temperature of the reaction flask was elevated to 310 °C for further growth of $Cd_{1-x}Zn_xS$ cores. After the elapse of 8 min of reaction, 8 mM of S powder dissolved in tributylphosphine (TBP, 90 %) were introduced into the reactor to overcoat existing $Cd_{1-x}Zn_xS$ cores with ZnS shells without any purification steps. Aliquots of QDs were taken during the reaction to analyze the development of QDs. After the reaction was completed, the temperature was cooled down to room temperature. QDs were extracted and purified by adding 20 ml of chloroform and an excess amount of acetone (done twice); then they were redispersed in chloroform or hexane for further characterization. In order to adjust the optical properties of QDs, the amount of S precursors in the first injection was varied maintaining the other entire parameters constant.

2.1.5 Organic Materials

4,4'-bis(carbazol-9-yl)biphenyl (CBP) as hole transport layer, 4,4',4''-tris(N-carbazolyl)-triphenylamine (TCTA) as hole transport layer are purchased from OSM. poly[(9,9-bis(3'-(N,N-dimethylamino)propyl)-2,7-fluorene)-alt-2,7-(9,9-ioctylfluorene (PFN) as conjugated polyelectrolyte layer was purchased from 1-Material Inc. Chemical structures of organic materials used in this thesis are as follows.

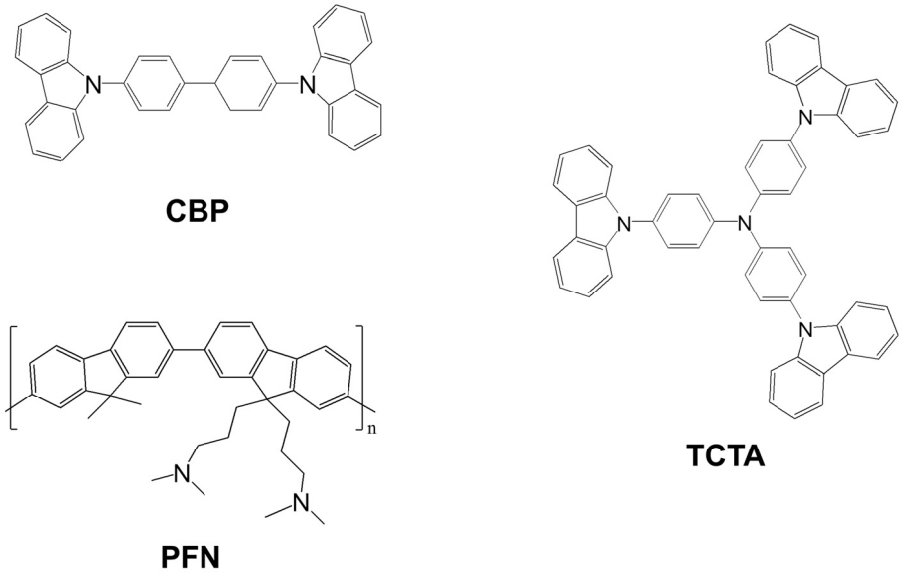

Figure 2.1 Chemical structures of CBP, TCTA and PFN

2.2 Device Fabrication and Characterization Methods

2.2.1 Device Fabrication

All QLED devices were basically fabricated using the inverted structures and the detail structures, materials and processes are introduced in each chapter. First of all, patterned ITO glass substrates were prepared, which were cleaned with acetone, isopropanol and deionized water in an ultrasonicator (Branson 5510). And then the cleaned ITO glass substrates were dried in the oven at 120 °C. For the inverted structure, 20 mg/mL of the ZnO nanoparticle solution was spin-coated on a patterned ITO glass with a spin-rate of 2000 rpm for 60 sec and dried at 90 °C for 30 min in the oven filled with N_2 gas. The thickness of ZnO layer as electron injection/transport layer was about 45 nm. QD solution was spun on the bottom layer at 4000 rpm for 30 sec, followed by baking in N_2 oven at a temperature of 70 °C.

2.2.2 Current-voltage-luminance Measurement

The current-voltage (I-V) characteristics were measured with a Keithley 236 source measurement unit, while the electroluminescence was measured with a calibrated Si photodiode (Hamamatsu, S5227-1010BQ) with a size of 10 mm × 10 mm placed at an angle normal to the device surface, assuming that the device was a Lambertian source. To detect a turn-on voltage of light-emitting diodes, we use an ARC PD438 photomultiplier tube (PMT) with the Keithley 236 source measurement unit. The electroluminescence (EL) spectra and the Commission Internationale de L'Eclairage (CIE) color coordinates were measured with a Konica-Minolta CS-1000A spectroradiometer. The luminance and efficiency were calculated from the photocurrent signal of photodiode with a Keithley 2000 multimeter, and corrected precisely with the luminance from CS-1000A.

The chromatic characteristics were calculated from EL spectra measured by the CS-1000A spectrometer using the CIE 1931 color expression system. The tristimulus values XYZ can be calculated by following equations,

$$X = K_m \int_0^\infty \bar{x}(\lambda) P(\lambda) d\lambda \quad (2.1)$$

$$Y = K_m \int_0^\infty \bar{y}(\lambda) P(\lambda) d\lambda \quad (2.2)$$

$$Z = K_m \int_0^\infty \bar{z}(\lambda) P(\lambda) d\lambda \quad (2.3)$$

where, P(λ) is a given spectral power distribution of emissive source, $\bar{x}$, $\bar{y}$ and $\bar{z}$ are the CIE standard color matching functions (see Figure 2.2) and Km is the weighing constant (683 lm W^{-1}). From the tristimulus values, the CIE color coordinates calculated by following equations,

$$x = \frac{X}{X+Y+Z} \tag{2.4}$$

$$y = \frac{Y}{X+Y+Z} \tag{2.5}$$

$$z = \frac{Z}{X+Y+Z} \tag{2.6}$$

Any color can be plotted on the CIE chromaticity diagram.

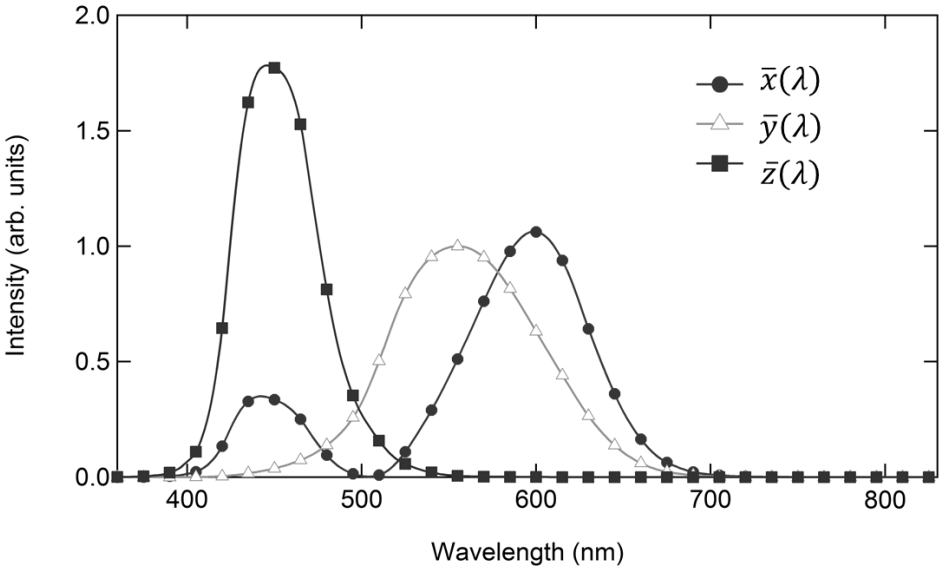

Figure 2.2 The CIE standard observer color matching functions

2.2.3 Efficiency Calculation Methods

To evaluate the emission properties of light-emitting diodes, the commonly employed efficiencies are the external quantum efficiency (EQE), the luminous efficiency (LE) and the power efficiency (PE).

The external quantum efficiency can be defined by the following equation.

$$\mathrm{EQE} = \frac{number\ of\ emitted\ photons}{number\ of\ injected\ electrons}(\%)$$

Typically, QLEDs or OLEDs emit light into the half plane due to the metal contact. Without any modification for increasing out-coupling efficiency, over 80% of the emission can be lost to internal absorption and wave-guiding in a simple planar light-emitting device.

Since human eye has different spectral sensitivity in visible area, the response of the eye is standardized by the CIE in 1924 (see $\bar{y}$ in Figure 2.2). The luminous efficiency weighs all emitted photons according to the photopic response of human eye. The difference is that EQE weighs all emitted photons equally. LE can be expressed by the following equation.

$$\mathrm{LE} = \frac{luminance}{current\ density}(cd\ A^{-1})$$

The luminance value (cd m^{-2}) can be easily measured by the commercial luminance meter (CS-1000A in this thesis).

The power efficiency is the ratio of the lumen output to the input electrical power as follows,

$$\mathrm{PE} = \frac{luminous\ flux}{electrical\ power}(lm\ W^{-1})$$

The EQEs can be useful to understand the fundamental physics for light emission mechanism, while the PEs can be useful to interpret the power dissipated in a light-emitting device when used in a display application [50].

2.2.4 Other Characterization Methods

UV-Visible Spectroscopy: The transmission and absorption spectra were measured with DU-70 UV/Vis Scanning Spectrophotometer (Beckman Coulter, Inc.) or Agilent 8454 UV-Vis. diode array spectrometer. In case of solution, materials were dissolved in toluene or chlorobenzene. For the film measurement, materials were spin-coated or evaporated thermally in the thickness of ~50 nm on quartz substrate. The reflectance spectra were measured by a Varian Cary 5000 spectrophotometer. The average transmittance (T_{avg}) was calculated by the following equation.

$$T_{\mathrm{avg}} = \frac{\int_{\lambda_1}^{\lambda_2} T(\lambda)\mathrm{d}\lambda}{\lambda_2 - \lambda_1} \tag{2.7}$$

Where $T(\lambda)$ is the transmittance as a function of the wavelength, T_{avg} was usually calculated by integrating $T(\lambda)$ from 400 nm (λ_1) to 800 nm (λ_2).

Ultraviolet Photoelectron Spectroscopy (UPS): The UPS spectra were performed using Kratos AXIS-NOVA, employing He I light source and a hemispherical analyzer. The valence band maximum (VBM) of the nanocrystals was calculated using the following equation.

$$VBM = 21.2\,eV - \left|E_{cutoff} - E_{onset}\right| \tag{2.8}$$

The conduction band minimum (CBM) value was obtained by using the VBM and the excitonic band gaps of QDs, estimated from the PL spectra of QDs.

Atomic Force Microscopy (AFM): Topography of each film was measured by XE-100 (Park Systems) AFM System. Most of the films were measured in non-contact mode with NCHR probe tip (320 kHz, 42 N m^{-1}) followed by image processing in XEI v.1.7.1.

Transmission electron microscopy (TEM): The TEM images of the QDs were obtained using a Tecnai TF30 ST at 200 KV to analyze their average size and size distribution. The energy dispersive x-ray (EDX) spectra of QDs were acquired through Si-Li detector of Oxford INCA Energy attached on main body of TEM. Low-coverage samples were prepared by placing a drop of a dilute toluene dispersion of QDs on a copper grid (300 mesh) coated with an amorphous carbon film. The composition of QDs was measured with inductively coupled plasma optical emission spectroscopy (Agilent ICP-OES 720).

Field-emission scanning electron microscopy (FE-SEM): ZnO nanoparticles films are investigated by SEM without any other treatment. The model for this experiment is Augura, Carl Zeiss.

Film Thickness Measurement: Ellipsometers (L2W15S830 with 632.8-nm He-Ne laser light, Gaertner Scientific Corp. and M2000D, Woollam) and an AFM (XE-100, Park Systems) were used for measuring the thicknesses of films

QDs' general characterization: A photoluminescence quantum yield (PL QY) was acquired in the comparison of their fluorescence intensities with those of primary standard dye solution (coumarin 545, quantum yied = 95 % in ethanol) at the same optical density (below 0.05) at same excitation wavelength (400 nm). For photoluminescence lifetime measurements, the samples were excited at 488nm (pulse width ~ 40 ps) at a repetition rate of 2 MHz. PL dynamics were measured using time-correlated single-photon counting (TCSPC) system that consists of avalanche photodiodes (timing resolution ~ 350 ps) and a multi-channel analyzer (Picoquant Hydraharp).

Chemical Composition Analysis on CdSe/$Zn_{1-X}Cd_XS$ QDs: For chemical composition of cations (i.e., Cd and Zn atomic ratio) in $Zn_{1-X}Cd_XS$ shell layers, we assumed that all series of QDs are perfect sphere with identical size. We estimated the composition ratios between Zn and Cd contents for each layers by taking account of the volume of nth shell layers (ΔVn, Eq. 2.9, see also Figure 2.2).

$$\Delta \mathrm{Vn} = \frac{4}{3}\pi\left({R_n}^3 - {R_{n-1}}^3\right), n = 1,2,3,\cdots 7\ (R_0 = core\ radius, 2\ nm) \quad (2.9)$$

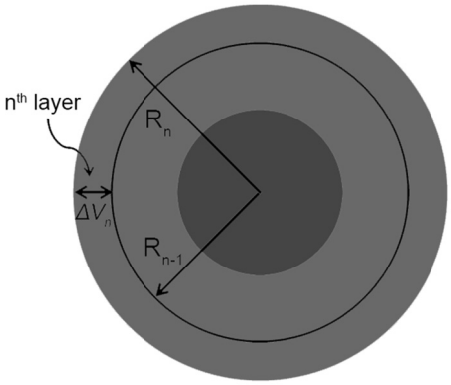

Figure 2.2 A schematic for chemical compositions within $Zn_{1-X}Cd_XS$ shells.

Chapter 3

Reducing Energy Transfer by Core/Shell Heterostructured Quantum Dots in QLEDs

Considerable effort has been devoted to improving the device efficiency and operational stability of QLEDs. In contrast, little attention has been paid to the structural design of the QDs themselves, and most of the endeavors have been dedicated to optimizing device architectures. Although the past few decades have witnessed remarkable progress in the efficiency and stability of such devices, fundamental issues from the materials perspective remain. For example, the efficiency roll-off at a high applied bias limits the reliable and efficient operation of QLEDs. Spectroscopic analyses combined with device characteristics have

suggested that electric-field-induced exciton dissociation [51, 52] and/or non-radiative Auger decay [35, 53] are responsible for the relatively poor device efficiency, including the efficiency roll-off behavior. In type-I core/shell heterostructured QDs, electron and hole wave functions are both confined to the core, effectively reducing exciton dissociation under the external electric field. [51] Nonetheless, typical type-I QDs with rather thin (1-2 nm) shells are still susceptible to becoming charged in actual devices, particularly at high current densities, resulting in substantial efficiency decrease and poor device stability. the use of quasi type-II "giant" QDs, [35, 54] in which Auger recombination is significantly suppressed by the concerted effects of volume scaling [55-58] and smoothing of the potential change at the core/shell interface, [35, 59, 60] has improved QLED performance. [35] However, the absolute device efficiencies and brightness in this case remain constrained by the relatively low single-exciton PL QY (~ 40 %) of the quasi type-II QDs.

Despite the implications of these previous studies, systematic efforts to correlate the shell thickness of type-I heterostructured QDs with QLED performance have been lacking. Although they are conceptually simple, such studies are complicated because the optical properties of QDs (e.g., PL energy, PL QY, and exciton and multicarrier dynamics) can vary dramatically as the shell thickness changes. [27, 30, 55, 56, 61] To minimize these issues, we used a successive growth method to prepare a series of highly luminescent CdSe/$Zn_{1-X}Cd_XS$ type-I heterostructured QDs featuring a constant CdSe core radius of 2.0 nm and varying shell thicknesses (total QD radius R = 4.5 – 8.3 nm). Direct comparison of the spectroscopic analysis results and device characteristics revealed that all such QDs

exhibit nearly identical PL energy, QY and lifetime in solution but that QD samples with thicker shells exhibit higher luminescence efficiencies in actual devices. We attribute this improved luminescence efficiency to the suppression of ET among neighboring QDs and reduced QD (negative) charging in QD solids under device operating conditions. As an ultimate achievement, we fabricated deep-red QLEDs that exhibited high device efficiency (peak EQE ~ 7.4 %) and record-high brightness (> 100,000 cd/m^2, peak emission @ 625 nm). Thus, we demonstrated that simple but novel structural engineering of core/shell heterostructured QDs can be used to optimize the optical properties of QD solids and, consequently, the performance of the resulting electroluminescent devices for display, lighting, or laser applications.

3.1 Design of core/shell heterostructures QDs with different shell thicknesses.

As a primary focus, we analyzed a series of core/shell heterostructures QDs with different shell thicknesses. We chose CdSe/$Zn_{0.5}Cd_{0.5}S$ QDs as a model system for type-I QDs because the mitigated lattice mismatch (7 %) between the CdSe core and the $Zn_{0.5}Cd_{0.5}S$ shell would allow for structural engineering with varying shell thicknesses. [61, 62] A series of CdSe/$Zn_{1-X}Cd_XS$ QDs with fixed CdSe core radius (r = 2.0 nm) and varying shell thicknesses were prepared *via* a one-pot successive growth method (Figure 3.1 and Figure 3.2). The QDs retained a regular shape, reasonable size distribution (σ < 13 %, as assessed by transmission electron microscopy [TEM], Figure 3.3) and narrow PL spectra (FWHM < 100 meV, Figure 3.2a) throughout the shelling progress, consistently with the successive growth of uniform $Zn_{1-X}Cd_XS$ layers at each shelling step. Elemental analysis *via* inductively coupled plasma-optical emission spectroscopy (ICP-OES) of successive shell thicknesses revealed that the innermost shells (shell thickness $H \leq 2.5$ nm) are slightly Cd-rich (~$Zn_{0.4}Cd_{0.6}S$), while the outer shells (2.5 nm $\leq H \leq$ 6.3 nm) were very similar to $Zn_{0.5}Cd_{0.5}S$ in composition (Table 3.1). Peaks in the absorption and PL spectra both shifted to lower energy (ΔE_{PL} = ~ 0.1 eV) during inner shell growth (Figure 3.2) because of a small degree of delocalization of the electron and hole wave functions into the $Zn_{0.4}Cd_{0.6}S$ shell. In contrast, the $Zn_{0.5}Cd_{0.5}S$ outer shell growth did not appear to alter the PL properties (*i.e.*, PL spectra, PL QY and PL dynamics, Table 3.2) or absorption at longer wavelengths (> 490 nm), suggesting that electron and hole wave functions are largely excluded from the $Zn_{0.5}Cd_{0.5}S$ outer shell.

Unlike the case of quasi type-II CdSe/CdS QDs, [35, 56] in which the hole wave function is strongly confined within CdSe cores and the electron wave function is delocalized over the entire volume, CdSe/$Zn_{1-X}Cd_XS$ QDs are type-I heterostructures. In other words, both electron and hole wave functions are confined within the CdSe core with an estimated energy band offset of 0.3 eV between the core and shell. [62] Because the additional growth of $Zn_{0.5}Cd_{0.5}S$ outer shell layers does not affect the wave functions of charge carriers confined in CdSe/$Zn_{0.4}Cd_{0.6}S$, the size (volume) dependency was not observed in peak PL energy, PL QY, and exciton dynamics among CdSe/$Zn_{1-X}Cd_XS$ QDs with varied outer shell thicknesses (2.5 nm ≤ H ≤ 6.3 nm). The optical properties and structural features of CdSe/$Zn_{1-X}Cd_XS$ QDs are summarized in Table 3.2: the main control parameter in our study was the size of the QDs, specifically the shell thickness.

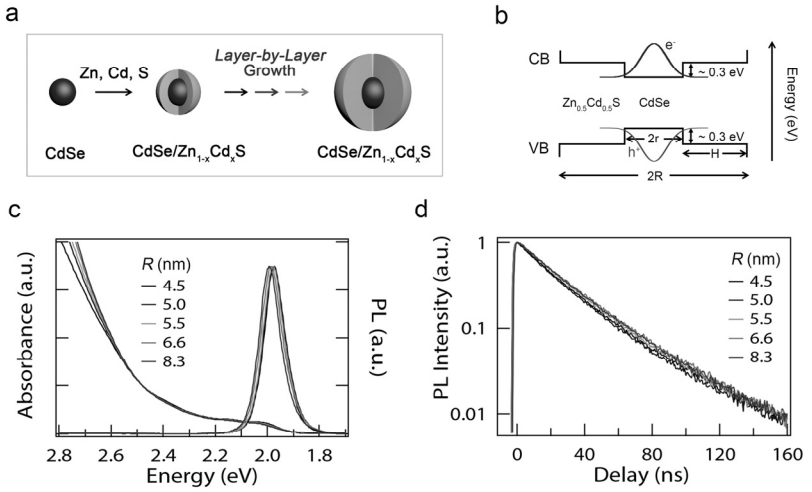

Figure 3.1 (a) Schematic illustration of CdSe/$Zn_{1-X}Cd_XS$ QD synthesis (b) Energy-band diagram, (c) UV-Vis and PL spectra of CdSe/$Zn_{1-X}Cd_XS$ QD with CdSe core radius (*r*) of 2.0 nm and different $Zn_{1-X}Cd_XS$ shell thicknesses [total radius, *R*]. (d) PL decay dynamics of same (QDs in solution).

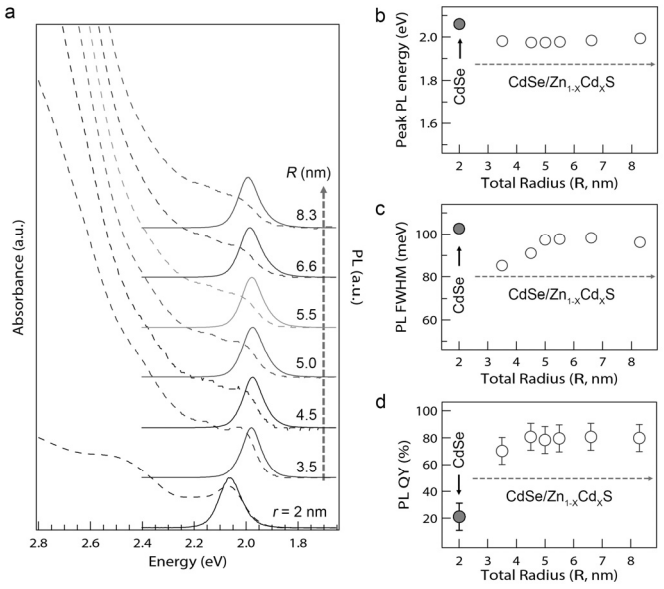

Figure 3.2 (a) Normalized absorbance and PL spectra of CdSe (r = 2.0 nm)/$Zn_{1-X}Cd_XS$ during the shell growth. (b) Peak PL energy, (c) full width at half maximum of PL and (d) PL QY of CdSe/$Zn_{1-X}Cd_XS$ QDs as a function of total radius R.

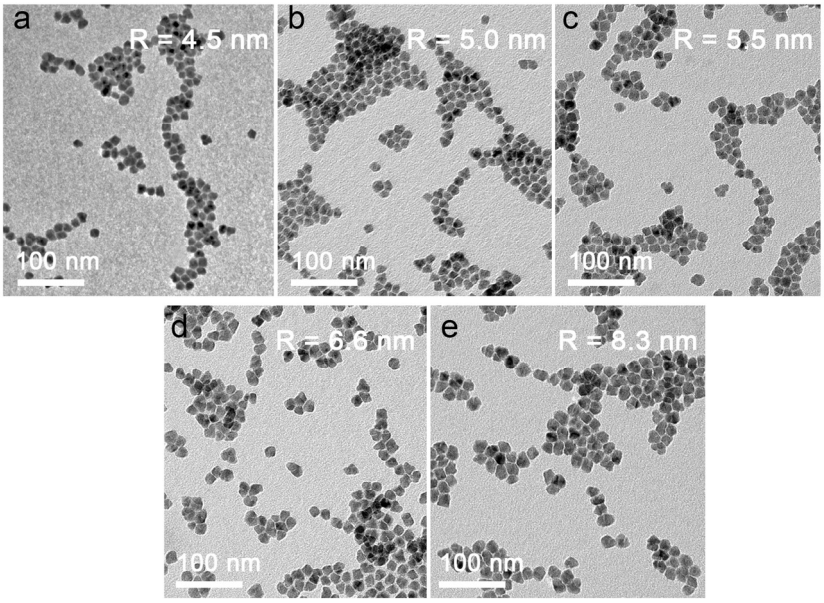

Figure 3.3 TEM images of CdSe/$Zn_{1-X}Cd_XS$ QD with CdSe core radius (*r*) of 2.0 nm and different $Zn_{1-X}Cd_XS$ shell thicknesses [total radius, *R*, varies from (a) 4.5 nm to (e) 8.3 nm]

Table 3.1 The chemical composition profile in CdSe/$Zn_{1-X}Cd_XS$ QDs.

Sample Size (R, nm)	[Cd] (mg/L)[a)]	[Zn] (mg/L)[b)]	Radius range (nm)	Cd contents (%)[c)]	Zn contents (%)[d)]
2.0	85 ± 1	0	0 - 2.0 (core)	100	0
3.5	449.2 ± 3	104.8 ± 0.6	2.0 – 3.5	62.6	37.4
4.5	1057 ± 4	318.7 ± 0.6	3.5 – 4.5	63.2	36.8
5.0	509.9 ± 1	261.3 ± 0.5	4.5 – 5.0	50.9	49.1
5.5	674.3 ± 1	356.0 ± 1	5.0 – 5.5	50.8	49.2
6.6	890.6 ± 2	450.2 ± 0.9	5.5 – 6.6	52.9	47.1
8.3	499.6 ± 1	255.7 ± 1	6.6 – 8.3	52.8	47.2

[a),b)]Chemical contents of QDs obtained from ICP-OES. [c),d)]Cation contents within the chosen range of radius calculated from the volume and the composition of QDs.

Table 3.2 Structural characteristics and optical properties of different sized CdSe/$Zn_{1-X}Cd_XS$ QDs.

QD notation	core radius(r) /shell thickness(H) (nm/nm)	total radius (R ± Std, nm)	Peak PL energy / FWHM (eV/meV)	PL QY (%)[a]	τ_x (ns)[b]	Ligands
4.5 nm QDs	2.0/2.5	4.5 ± 0.65	1.97 / 91.1	81	26.0	Oleic acid
5.0 nm QDs	2.0/3.0	5.0 ± 0.64	1.97 / 97.4	79	25.3	Oleic acid
5.5 nm QDs	2.0/3.5	5.5 ± 0.65	1.98 / 97.7	80	26.7	Oleic acid
6.6 nm QDs	2.0/4.6	6.6 ± 0.75	1.98 / 98.3	81	28.1	Oleic acid
8.3 nm QDs	2.0/6.3	8.3 ± 0.95	1.99 / 96.2	80	27.7	Oleic acid

[a)] PL QY was measured using a spectrometer with an integrating sphere; [b)] τ_x denotes the time when PL intensity becomes 1/e of initial PL intensity.

3.2 Characteristics of electroluminescence devices made of a series of $CdSe/Zn_{1-X}Cd_XS$ QDs

The "inverted" QLED architecture [ITO (150 nm)//ZnO (40 nm)//QDs (20 nm, 1-2 monolayers)//CBP (60 nm)//MoO_X (10 nm)//Al (100 nm), Figure 3.4a] was chosen for this study not only because this specific device architecture exhibits the record efficiency (EQE ~ 18 %) [10] but also because it does not require chemical changes (*i.e.*, ligand exchange) to be applied to the QD active layer. [9] To fabricate the devices, QD layers were similarly cast from solution (20 mg ml^{-1} in hexane) directly on ZnO//ITO. The CBP, MoO_3 and Al were thermally evaporated at a deposition rate of 1 ~ 2 Å/sec for CBP, 0.5 Å/sec for MoO_3, and 4 ~ 5 Å/ sec for Al electrode. The device operates *via* direct exciton formation within QDs by using the injected charge carriers from neighboring charge transport layers (CTLs) [10, 53], as depicted in Figure 3.4b.

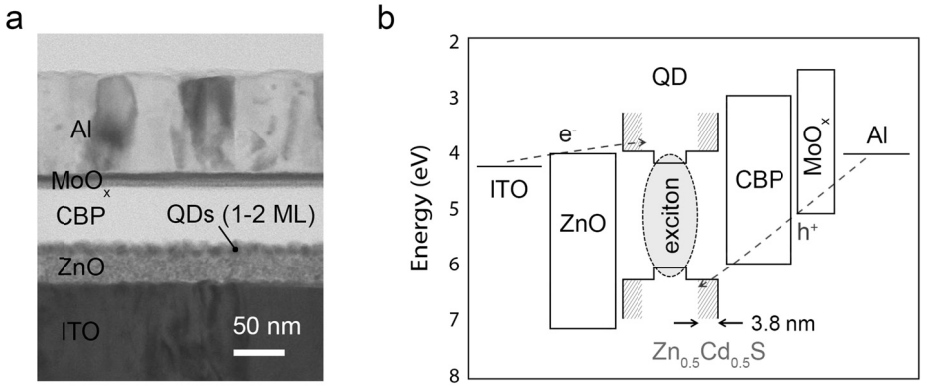

Figure 3.4 Characteristics of electroluminescence devices made of a series of $CdSe/Zn_{1-X}Cd_XS$ QDs (r = 2.0 nm, R = 4.5, 5.0, 5.5, 6.6 and 8.3 nm). (a) Cross-sectional TEM image and (b) energy band diagram of electroluminescent device with $CdSe/Zn_{1-X}Cd_XS$ QDs.

All QLEDs showed the EL solely from the QDs under the full range of current densities (Figure 3.5a), thus validating the direct exciton formation within QD active layers. Regardless of the QD size, the QLEDs in this study displayed typical diode behavior and showed similar turn-on voltages (V_{ON} ~ 2 eV, Figure 3.5b) near the optical bandgap of the QDs, implying that the $Zn_{0.5}Cd_{0.5}S$ shell presents no more than a marginal potential barrier to charge carrier injection into QDs. In contrast to the electrical properties, substantial size-dependencies were observed in the luminance and EQE curves. QLEDs incorporating larger QDs with thicker shells exhibited higher EQEs and greater brightness under the same current density (Figure 3.5b-c, Table 3.3). Specifically, QLEDs based on 8.3-nm QDs exhibited a peak EQE of 7.4 % and a brightness exceeding 100,000 cd/m^2, corresponding to a 2-fold increase in EQE and a 4-fold increase in maximum brightness, respectively, compared with QLED including 4.5-nm QDs.

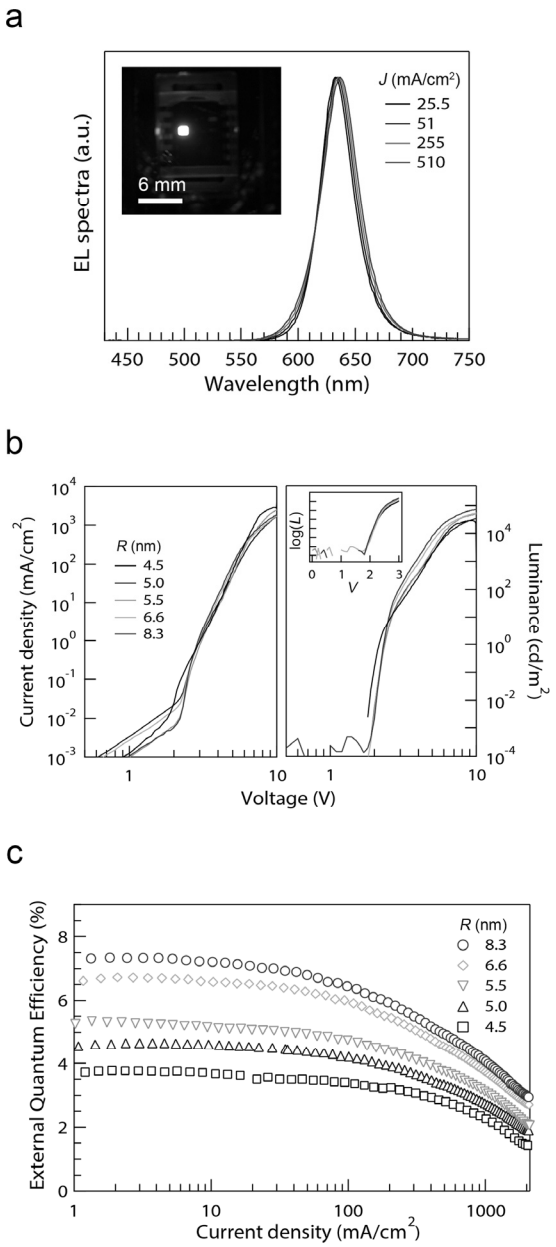

Figure 3.5 (a) Normalized current-dependent electroluminescence spectra of a QLED with 8.3 nm QDs (inset: a photograph of an operating device at 3 V), (b) current density-voltage-luminance curves and (c) EQE *versus* current density graphs for QLEDs based on CdSe/$Zn_{1-X}Cd_XS$ QDs of varied total radius, *R*.

Table 3.3 Characteristics of QLEDs incorporating different sized CdSe/$Zn_{1-X}Cd_XS$ QDs.[a]

QD notation	V_{on} (V)	Peak EL energy (eV)	Peak EQE (%)	Max. L (cd/m^2)	@ 1,000 cd/m^2		$\langle N \rangle_{E,1/2EQE}$	CIE index (x, y)
					J (mA/cm^2)	V (V)		
4.5 nm QDs	2.0	1.94	3.5	27,233	46.7	5.7	0.163	(0.701, 0.298)
5.0 nm QDs	2.0	1.95	4.7	47,984	27.9	4.6	0.195	(0.698, 0.302)
5.5 nm QDs	2.0	1.96	5.4	61,125	19.8	4.5	0.232	(0.694, 0.305)
6.6 nm QDs	2.0	1.96	6.7	85,022	15.5	4.1	0.288	(0.695, 0.305)
8.3 nm QDs	2.0	1.98	7.4	105,870	10.2	3.7	0.378	(0.688, 0.311)

[a] Abbreviations: turn-on voltage (V_{ON}), voltage (V), luminance (L), current density (J), and average exciton number at the half peak EQE ($\langle N \rangle_{E,\,1/2EQE}$).

3.3 Influence of QD shell thickness on the optical properties of QD films and the efficiencies of corresponding devices

To elucidate how the shell thickness of type-I QDs correlates with QLED performance, we measured the PL-decay dynamics of QD films and related the characteristic decay time to the device efficiency. Figure 3.6a plots the PL decay dynamics of the series of QD film samples (1-2 monolayers) within the actual devices. As shown in Figure 3.1d, Table 3.2 and Figure 3.6b, PL lifetimes were nearly constant in solution (~ 28 ns), regardless of the shell thickness, because of the localization of both electrons and holes within the CdSe core. However, the PL lifetimes drastically decreased when QDs were assembled into compact films and decreased further within the actual devices (Figure 3.6b), and the severity was clearly dependent on shell thickness (*i.e.*, the thinner the shell, the more dramatic the lifetime reduction). Interestingly, this tendency was markedly similar to the absolute PL QYs measured from the same samples using an integrating sphere spectrometer; in fact, for both "on glass" and "in device" samples, the size-dependent relative decreases of PL lifetime and PL QY were approximately the same. The similarity between the two independent measurements for the series of CdSe/$Zn_{1-X}Cd_XS$ QDs suggests that fast, non-radiative fast decay pathways are active when QDs are assembled in solid films and that their contributions become more pronounced as QDs are incorporated into real devices.

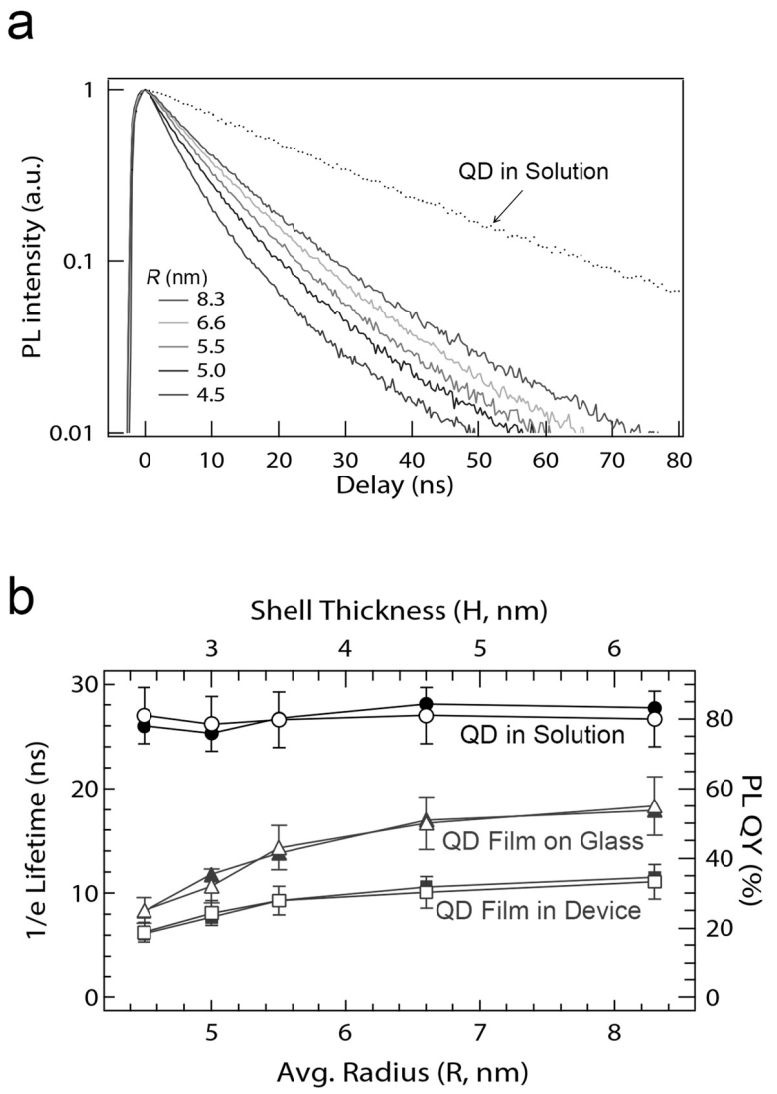

Figure 3.6 (a) PL decay dynamics of CdSe/$Zn_{1-X}Cd_XS$ QD active layers in electroluminescent devices. PL decay dynamics of CdSe/$Zn_{1-X}Cd_XS$ QDs (r = 2.0 nm, R = 8.6 nm) in solution is displayed for comparison. (b) 1/e lifetime (filled) and PL QY (empty) of QD solutions (circles), QD films on glass substrates (triangles) and QD films in actual devices (squares).

In QD solids, excitons are known to diffuse *via* QD-QD ET, in some cases over distances exceeding 30 nm. [63] During sequential ET processes, excitons are subject to the non-radiative decay pathways available in any involved QD, resulting in net reduction of the PL QY in any sample in which the occurrence of ET is significant. [53] We quantified the ET losses by measuring QDs assembled on glass substrates. We assumed that the dots were partitioned into two possible cases of "dark" and "bright" QDs (see Figure 3.7). In other words, "dark" QDs exhibit "ET", and "bright" QDs are identical to "radiative" QDs. However, the non-radiative losses in "dark" QDs were so fast that they could not be resolved in our measurements. This assumption yields the following equation relating the PL QY in films (QY_f) to that in solutions (QY_0).

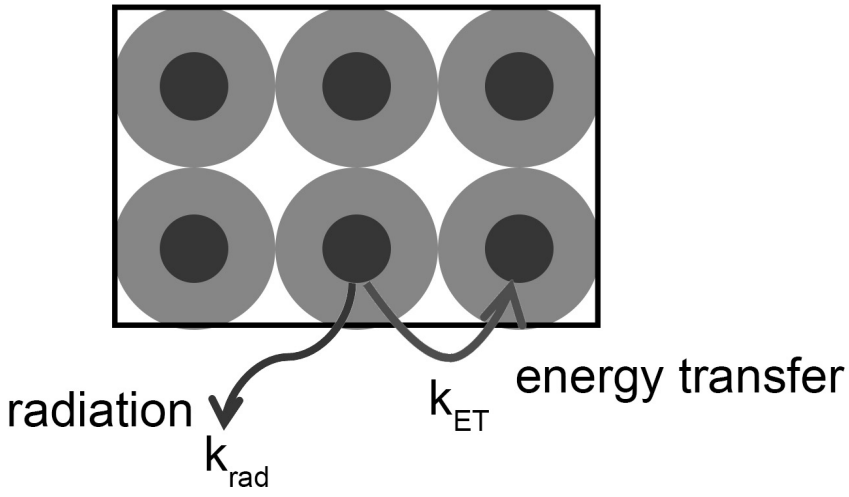

Figure 3.7 A schematic illustration of two possible cases in the inverted QLEDs

$$QY_f = QY_0 \times \frac{k_{rad}}{k_{rad} + k_{ET}} + QY_0 \times \left(1 - \frac{k_{rad}}{k_{rad} + k_{ET}}\right) \times QY_0 \times \frac{k_{rad}}{k_{rad} + k_{ET}} + (QY_0 \times (1 - \frac{k_{rad}}{k_{rad} + k_{ET}}))^2 \times QY_0 \times \frac{k_{rad}}{k_{rad} + k_{ET}} + \cdots$$

where,

$$k_{rad} = \frac{1}{\tau_{rad}} k_{ET} = \frac{1}{\tau_{ET}}$$

(3.1)

From Equation (3.1), the first term represents the PL QY of a QD, when one QD emits light without ET, and the second term represents the case in which one QD consumes its energy not through radiative recombination but through transferring its energy to adjacent QDs. Similarly, the third term and the others follow the above-described pattern. Mathematically, Equation (3.1) becomes Equation (3.2).

$$\therefore QY_f = QY_0 \times \frac{k_{rad}}{k_{rad} + k_{ET}(1 - QY_0)}$$

(3.2)

This expression can be re-interpreted in terms of the effective non-radiative rate (k_{eff_nr}) in the sub-ensemble of "bright" dots in the case of ET.

$$k_{eff\_nr} = k_{ET}(1 - QY_0) \tag{3.3}$$

Equations (3.2) and (3.3) allow estimation of k_{ET} through two approaches: (1) based on the PL QY in QD films on glass substrates; and (2) based on the lifetimes measured on glass substrates, assuming that the total rate in this case is

$$k_{rad} + k_{eff\_nr}$$

Table 3.4 summarizes the characteristic values, such as QD diameter, and the various QYs and decay times of the samples.

Table 3.4 Characteristics of QD films made of different sized CdSe/$Zn_{1-X}Cd_XS$ QDs.

QD notation	D[a](nm)	QY_0[b]	QY_f	QY_d
4.5 nm QDs	11.0	0.81	0.25	0.19
5.0 nm QDs	12.0	0.79	0.32	0.24
5.5 nm QDs	13.0	0.80	0.43	0.28
6.6 nm QDs	15.2	0.81	0.50	0.30
8.3 nm QDs	18.6	0.80	0.55	0.33

τ_0[c] (ns)	τ_f (ns)	τ_d (ns)	$\tau_{ET\ QY}$[d] (ns)	$\tau_{ET\ lifetime}$[e] (ns)	τ_{qu}[f] (ns)
26.0	8.3	6.1	2.2	2.3	22.6
25.3	11.8	7.7	3.6	4.6	22.0
26.7	13.8	9.3	6.2	5.7	28.3
28.1	17.0	10.6	8.6	8.2	28.2
27.7	17.9	11.5	12.2	10.1	32.2

[a] D: center-to-center distance, $2R$ + 2 nm (based on a ligand length of ~1 nm); [b] QY_0, QY_f and QY_d denote the absolute PL QYs of solutions, films on glass substrates and in devices measured with an integrating sphere spectrometer, respectively; [c] τ_0, τ_f and τ_d denote the time when PL intensity becomes 1/e of initial PL intensity for solutions and films on glass substrates and in devices, respectively; [d] τ_{ET_QY} is derived from comparison of QY_f and QY_0; [e] $\tau_{ET\_lifetime}$ is derived from the analysis of τ_f and $\tau_{0;}$ [f] τ_{qu} is derived from the analysis of τ_d and τ_f.

ET is very sensitive to the interparticle distance between adjacent cores (in which electron and hole wave functions are delocalized), i.e., QDs with a thinner $Zn_{1-X}Cd_XS$ shell are likely to show more efficient ET in a film, as shown in Figure 3.8a. For core-to-core distances up to 13 nm, the characteristic ET times follow a D^6 dependence, whereas beyond that, the ET times scale as D^2. The transition from one type of separation dependence to another implies that ET occurs *via* Förster resonance ET (FRET) when the QD cores are in relative proximity and *via* reabsorption-and-emission as the dipole-dipole separation increases. As shown in Figure 3.6b and Table 3.4, the incorporation of QD films in devices causes additional quenching of QDs. We speculate that additional ET from QDs to the electrodes[64] may be responsible for the further reduction in PL Qys of QD active layers.

In Figure 3.8b, the PL Qys of QD layers are plotted versus the internal quantum efficiencies (IQEs) of the corresponding devices. The IQEs are estimated by dividing the peak EQEs at current densities of 1 mA/cm^2 (~ 3 V) with an estimated out-coupling factor (ca. 0.2). [16] The IQEs of devices are in remarkable agreement with the PL Qys of the corresponding QD active layers, implying that the PL QY of the QD active layer is essentially the determining factor for the peak EQEs of corresponding devices. This remarkable situation in which the device EQE is limited only by PL Qys is a result of the combination of specific advances in both the device architecture and the QD structure. The inverted device structure enables device operation at a low turn-on voltage that is nearly identical to the optical bandgap of QDs, [9, 10] thus minimizing the external electric field across QDs and any consequential exciton dissociation within QDs. [52] In addition, $Zn_{1-X}Cd_XS$ shells provide an energetic barrier for electron injection from ZnO into QDs, [35] impeding QD charging near the on-set voltage (V_{ON}). The result is QLEDs with

internal efficiencies determined solely by the PL efficiencies of the QD films within the devices.

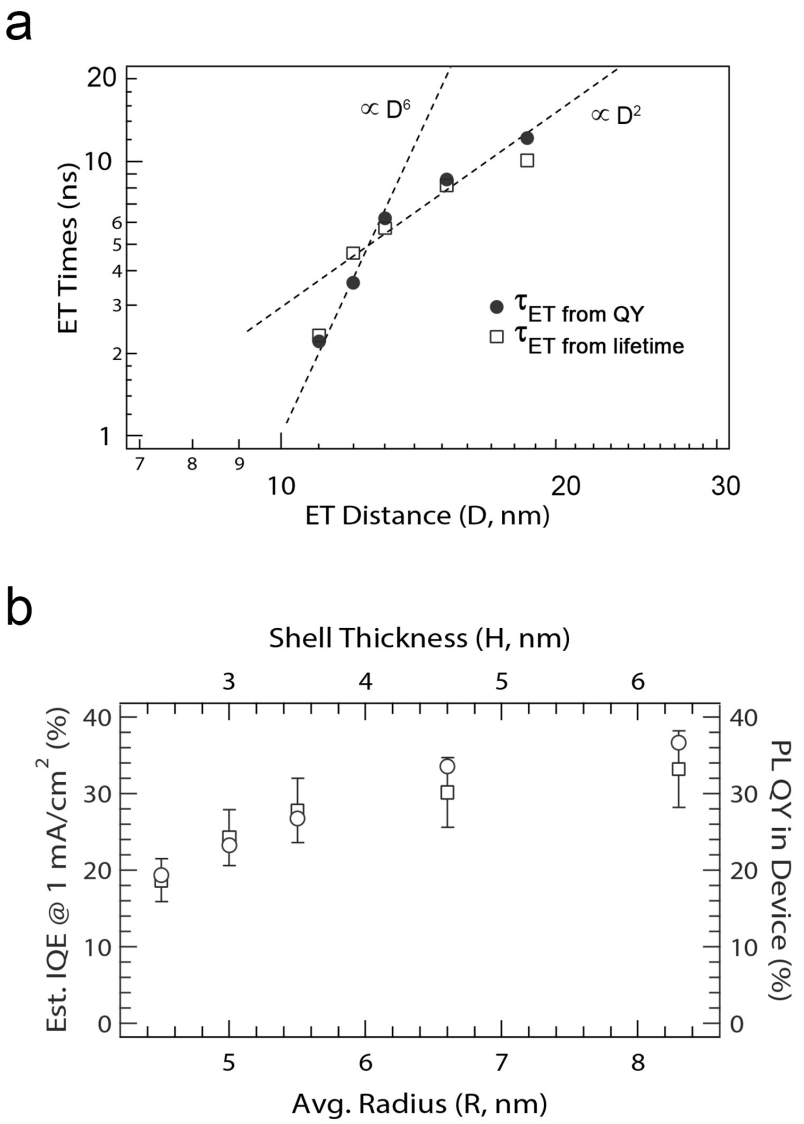

Figure 3.8 (a) Calculated energy transfer times from the PL QYs (filled circle) and the 1/e lifetimes (empty square) as a function of center-to-center distances [$D = 2R +$ 2 ligands (nm)]. (b) Estimated IQE at 1 mA/cm^2 (~ 3V, circles) and PL QY of QD films (square) in a device configuration.

3.4 Device characteristics plotted after consideration of absorption by individual QDs

As the $Zn_{1-X}Cd_XS$ shell thickness increases, the total number of QDs per unit area of the active layer in a device decreases (Figure 3.9). In other words, we must consider how many QDs contain injected charge carriers in the fixed pixel area and how many charge carriers are injected into the individual QDs. from the fact that thick-shell QDs give higher brightness indicates that such QDs are more efficient at producing a photon from each exciton compared to those with a thin shell.

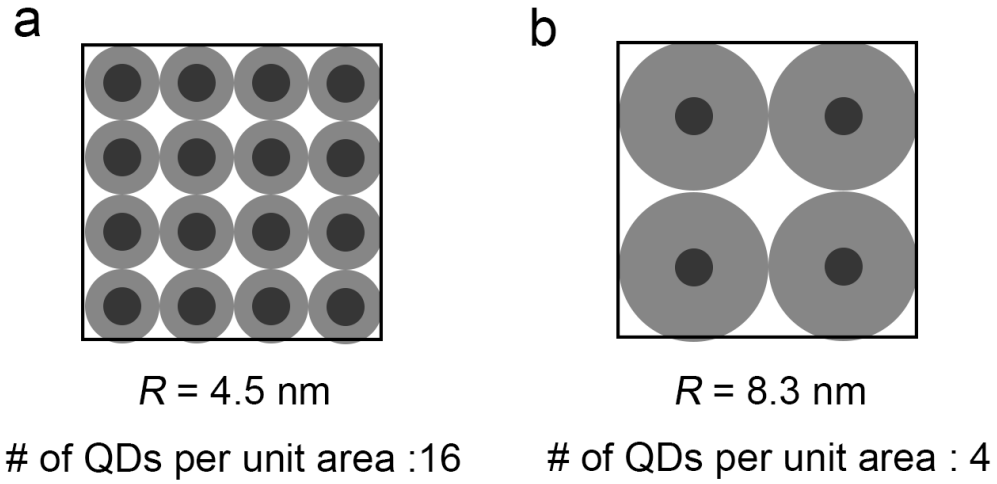

Figure 3.9 A schematic illustration of different total numbers (#) of QDs with different shells packed in active layer in QLEDs

To understand how device EQE is related to the exciton occupancy of individual QDs in the active layer, we analyzed the device characteristics as a function of the average exciton number, $\langle N \rangle_E$, induced by electron-hole injection (Figure 3.10). For simplicity, we assume that all individual QDs in a sample set are identical in size and have the same optical properties. The average exciton number

produced *via* electrical pumping is calculated using the coupled rate equation as described below. [65]

The average exciton number under continuous electrical pumping can be obtained by considering coupled rate equations. For simplicity, we consider only three energy levels of a QD: ground, exciton, and biexciton states. The population changes in each level can be expressed as,

$$\frac{dn_0}{dt} = \frac{n_1}{\tau_1} - G_E n_0$$

$$\frac{dn_1}{dt} = G_E n_0 + \frac{n_2}{\tau_2} - \frac{n_1}{\tau_1} - G_E n_1$$

$$\frac{dn_2}{dt} = G_E n_1 - \frac{n_2}{\tau_2}$$

where n_0, n_1, and n_2 are the probabilities that the QD is found in the ground, exciton, and biexciton states with a constraint of $n_0 + n_1 + n_2 = 1$. G_E is the exciton generation rate that is defined as the current density divided by QD density, and τ_1 (τ_2) is the decay constant of exciton (biexciton). In steady state, we can find the following:

$$n_0 = \frac{1}{1 + G_E\tau_1 + G_E^2\tau_1\tau_2}$$

$$n_1 = n_0 G_E \tau_1$$

$$n_2 = n_0 G_E^2 \tau_1 \tau_2$$

Thus, the average exciton number is given,

$$\langle N \rangle_E = n_1 + 2n_2 = \frac{G_E\tau_1(1 + 2G_E\tau_2)}{1 + G_E\tau_1 + G_E^2\tau_1\tau_2}$$

Because $\tau_1 \gg \tau_2$ (τ_1 = 28 ns, τ_2 = 50 ps for the present QDs), we can reduce the equation to

$$\langle N \rangle_E = \frac{G_E \tau_1}{1 + G_E \tau_1}$$

Figure 3.10a shows plots of the EQEs of QLEDs containing different-sized CdSe/$Zn_{1-X}Cd_XS$ QDs as a function of $<N>_E$ in individual QDs. Indeed, devices based on larger QDs exhibited higher efficiencies and suppressed efficiency roll-off not only in terms of current density but also as a function of exciton density (Figure 3.10b, Table 3.3). We quantified this observation by using the value $<N>_{E,1/2EQE}$, which represents the exciton density at which the EQE of a given QLED has fallen to ½ the peak value: $<N>_{E,1/2EQE}$ for QLEDs based on 8.3-nm QDs is 2.3 times higher than that of 4.5-nm QDs. These results reveal that QDs with thicker $Zn_{1-X}Cd_XS$ shells are more efficient than smaller QDs at exciton-to-photon conversion, even at relatively high exciton-generation rates.

We attribute the size dependence observed for the EL efficiency to the different degrees of QD charging at varying shell thicknesses (*H*). In the chosen device configuration, the electron injection from ZnO//ITO into QDs outpaces the hole injection from CBP//MoO_X//Al into QDs. [9, 10, 35] The accumulation of excess charge carriers (electrons) would result in (negative) QD charging and subsequent decreases in the EL efficiencies of individual QDs *via* Auger recombination. [35] The insertion of thick $Zn_{1-X}Cd_XS$ shells hinders electron injection rates by extending the distance between ZnO and the effective cores of QDs and reduces the extent of excess electron accumulation within QDs over the varied exciton generation rates. As a result, QDs with thicker $Zn_{1-X}Cd_XS$ shells displayed higher EL efficiencies and reduced efficiency roll-off characteristics over a wide range of exciton-generation rates.

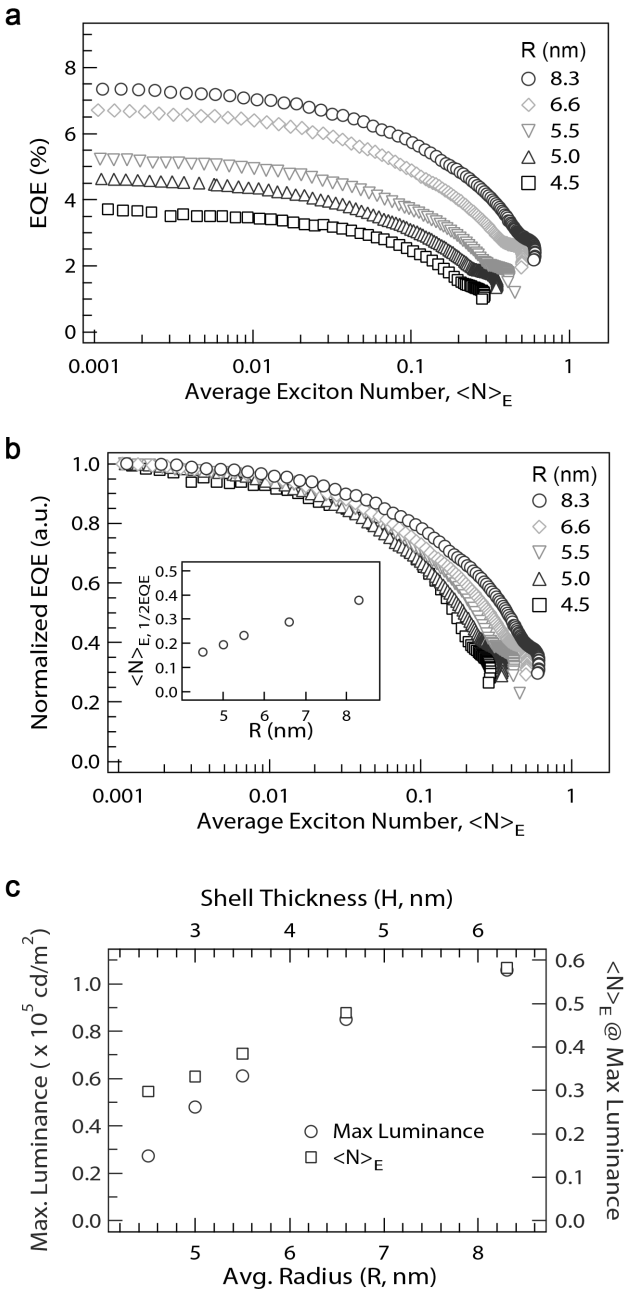

Figure 3.10 (a) Absolute and (b) normalized EQE of QLEDs as a function of $\langle N \rangle_E$. (inset: $\langle N \rangle_{E,1/2EQE}$ *versus* total radius). (c) Max luminescence and corresponding $\langle N \rangle_E$ of QLEDs.

Notably, the most efficient devices, namely the QLEDs based on 8.3-nm QDs, exhibited exceptionally high brightness (> 100,000 cd/m^2) in the d–ep-red spectral region [peak EL @ 630 nm, CIE index: (0.688, 0.311)]; in fact, this brightness is five times higher than that of our QLEDs based on 4.5-nm QDs (Table 3.3), i.e., twice the previous record QLED brightness (50,000 cd/m^2, peak EL @ 615 nm) [10] and comparable to the brightness of state-of-the-art OLEDs. [66] Key to this achievement is that thick $Zn_{1-X}Cd_XS$ shells not only dramatically increase peak EL efficiency but also provide efficiency and stability at the high current densities necessary to achieve maximum brightness.

Spectroscopic analysis of the QLEDs revealed the influence of non-radiative recombination processes on the overall device characteristics. The samples studied in this work had nearly identical PL energy and QY and thus would be expected to have similar (small) trap-related recombination losses. However, QLEDs based on thicker-shell QDs had markedly enhanced efficiency, which can be attributed to the suppressed ET in solid films, and reduced QD charging in operating devices. Because QD-charging and subsequent Auger recombination remained active in these QDs, particularly at high currents, a critical next step toward high-performance QLEDs is to engineer QDs with both suppressed charging and reduced Auger recombination efficiency.

We believe that the combination of methods for Auger suppression [35, 67] and strategies for improving charge injection balance (whether by using QDs with thick inorganic passivation layers or perhaps double-heterojunction QDs [68]) will eventually result in the necessary efficiency band brightness enhancements for QLEDs to be used in lighting and lasing applications.

3.5 Relationship between optical properties of QDs and the operational stability of corresponding devices

In addition to the peak efficiency and roll-off characteristics, the QD shell thickness influences the operational stability of devices. Figure 3.11 plots the normalized luminance intensity decay of QLEDs employing two different-sized QDs (4.5-nm QDs and 8.3-nm QDs) under operation (applied voltage: 3.7 V). Both QLEDs demonstrated a sharp efficiency drop during early operation and a subsequent gradual decrease in efficiency. Specifically, during the 35-hour operation, a QLED with 8.3-nm QDs exhibited 15 % initial efficiency reduction and 35 % subsequent efficiency decrease, and a QLED with 4.5-nm QDs displayed a drastic 40 % efficiency drop in the early stage and 15 % gradual decrease.

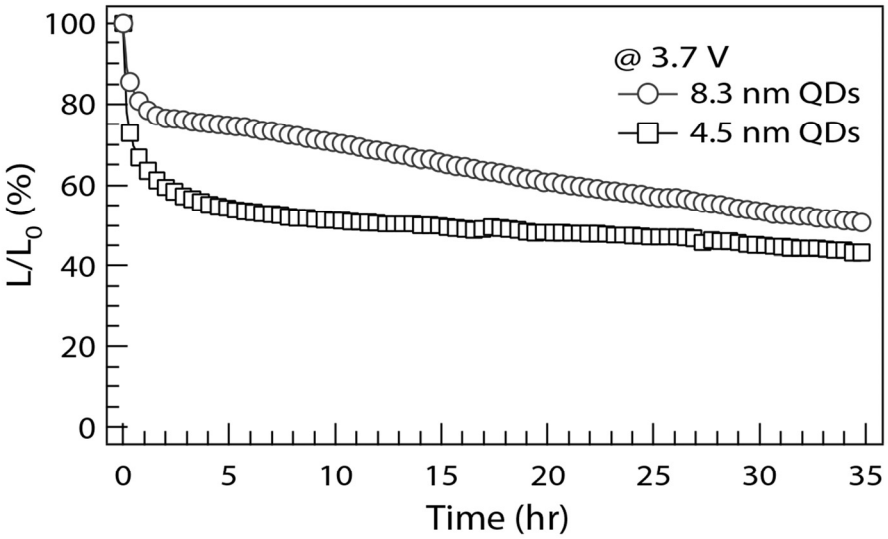

Figure 3.11 Normalized luminance curves of QLEDs with 4.5 nm QDs (square) and 8.3 nm QDs (circle) operated under 3.7 V.

To better understand device operational stability, we conducted optical characterization of QD active layers (Figure 3.12). During a 10-minute operation, QDs showed an abrupt reduction in the PL efficiency and the exciton decay dynamics, essentially indicating the rise of fast, non-radiative exciton decay pathways in QD active layers during device operation. The extent of PL efficiency reduction was proportional to the EL efficiency drop over the same timeframe, suggesting that the PL efficiency reduction of QD active layers causes the initial drop in device efficiency. The optical properties of QDs partially recovered when the applied voltage was set to 0 V. The reverse bias drove this recovery, but the efficiency did not return to the initial value. The spectroscopic results suggest that the initial EL efficiency decrease results from PL efficiency reduction in QD active layers from two different origins. We attribute the PL efficiency drop to QD degradation and QD charging. QDs are susceptible to chemical damage on their surfaces from charge carriers and joule heating, leading to decreases in their efficiency. In addition, during device operation, the excess charge carriers (electrons) steadily accumulate within QDs until the system reaches equilibrium and the exciton recombination efficiency decreases accordingly *via* Auger recombination. The $Zn_{1-X}Cd_XS$ shell thickness determines the influence of the surface traps on the effective cores and the extent of QD charging, = thus leading to the size dependence of the initial PL (EL) efficiency drop. After the initial efficiency drop, the optical properties of QD active layers did not change during operation (Figures 3.12b and c), whereas the device efficiency gradually decreased with operation time. Thus, the degradation of the CTLs, not the QDs, is the principal reason underlying the gradual efficiency decrease after the initial efficiency drop.

The device characteristics combined with the spectroscopic analysis consistently show that the PL efficiencies of QD active layers are the decisive factor controlling the device efficiency. In addition to the intrinsic optical properties, the ET processes and the QD charging substantially influence the PL efficiencies of QD active layers and, consequently, device performance. Among the chosen type-I sample series, which have similar optical properties and structural features except for the shell thickness, QDs with thicker shells are less likely to undergo the exciton transfer by either radiative (reabsorption) or non-radiative (FRET) processes and QD charging. In addition, QDs with thicker shells are less influenced by the surface trap states and additional QD charging during operation. Together, these results show that QDs with thicker shells can serve as efficient active layers in actual devices during operation, leading to significant improvements in the efficiency and operational stability of devices.

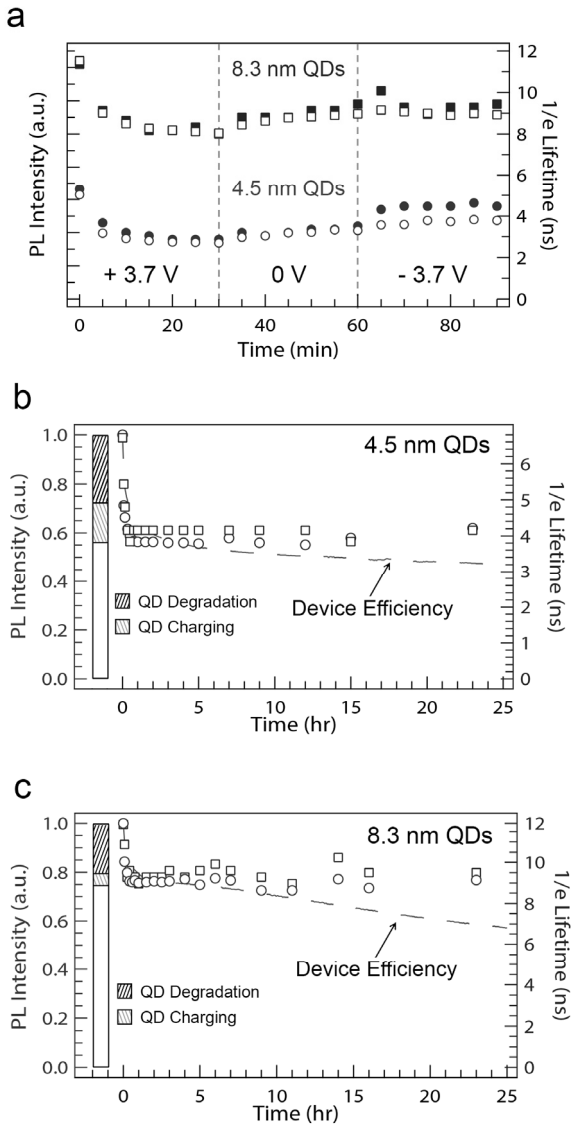

Figure 3.12 (a) PL intensity (solid) and 1/e lifetime (empty) of 8.3 nm QDs (square) and 4.5 nm QDs (circle) within the devices operated under forward bias (3.7 V), static (0 V) and reverse bias (-3.7 V). Normalized PL intensity (circle) and 1/e lifetime (square) of (b) 4.5 nm QD active layers and (c) 8.3 nm QD active layers within devices as a function of operation time. The operational device efficiencies (broken line) are overlaid for comparison.

3.6 Summary

In summary, we probed the influence of the shell thickness of type-I heterostructure QDs on QLED performance. We prepared a series of CdSe/$Zn_{1-X}Cd_XS$ core/shell type-I QDs with similar optical properties and the same CdSe core radius (2.0 nm) but different $Zn_{1-X}Cd_XS$ shell thicknesses (4.5 nm ≤ total radius ≤ 8.3 nm) by the *layer-by-layer* growth method. Systematic investigation of QLEDs and spectroscopic analysis of QD films suggest that thick-shell QDs exhibit reduced Auger-type decay rates and suppressed ET within QD solids. The photophysical changes are responsible for lessening the efficiency roll-off and improving the stability of QLEDs. These findings were confirmed by the device characteristics: high device efficiency (peak EQE ~ 7.4 %) and record-high brightness (105,870 cd/m^2), along with improved device stability. The approach and results used in this study suggest a simple but novel structural design of core/shell heterostructure QDs to allow the engineering of the optical properties of QD solids and the performance of the corresponding devices; in addition, they suggest rational guidelines for the practical use of QLEDs in high-power light sources.

Chapter 4

Improved Performance of Inverted Blue QLEDs by Adopting Double Electron Transport Layer

Most recent studies on QLEDs have focused on understanding QD device physics and modification of the material architecture to address the limits of device performance. However, the issues of device performance, which can be attributed to multicarrier effects and charge imbalance, remain unclear. Despite recent rapid developments, formidable issues remain to be overcome. In inverted systems, the metal oxide nanoparticle film quality and properties are key factors for the improvement of QLEDs. Typically, the compactness of the metal oxide nanoparticle films is not perfect compared to that of small molecule organic films and polymer

organic films. In organic optoelectronic devices using a metal oxide layer as the CTL, many efforts have been made to cover porous metal nanoparticle films and smooth rugged thin-film layers. [69-71] The leakage current generated from pin-holes in the deposited film decreases the performance of organic-–inorganic hybrid devices (e.g., OLEDs, organic solar cells, organic TFTs and hybrid LEDs). Despite previous studies' implications regarding electron confinement and control of electron injection into the QD core, [14, 35] charging obstacles, which inhibit bright emission in QDs, remain challenging for various reasons. Herein, we demonstrate the production of efficient QLEDs employing a double ETL (i.e., inorganic ETL//organic ETL) for passivating the porous metal oxide layers, controlling the charge injection into the emissive layer, and reducing exciton quenching *via* non-radiative recombination.

4.1 Preparation of double electron transport layers

By applying the improved ETLs in blue QLEDs, we passivated the ZnO nanoparticle films. As shown in the SEM images in Figure 4.1a, the surface morphology of the ZnO nanoparticle films contains several pin-holes or valley-shaped holes. These flaws in the inorganic films can affect the device performance; for example, leakage current resulting from these flaws can decrease the lifetime of blue QLEDs. In other words, the leakage current arising from the short distance between the cathode and QDs layer degrades device performance. To cover the film vacancies and defects, blending organic materials and nanoparticles may be not the best method to improve film quality, because nanoparticle materials are massively phase-separated or aggregated from organic materials. [48] Although the separation of mixed layers would effectively smooth the tops of ZnO layers, the aggregation of mixed ETLs may hinder electron injection from ITO into ZnO. As a result, we formed a double ETL by spin-coating one or more organic layers between the ZnO layer and the QD layer. Figure 4.1b confirms the successful coverage of the double ETL (ZnO//TPBI). Comparison of the SEM image of the ZnO nanoparticle films alone and that of ZnO//TPBI (Figure 4.1) revealed that the surface roughness and morphology were compensated for by the additional layers. Because TPBI was dissolved in chlorobenzene, orthogonality was guaranteed in the ZnO and TPBI bi-layers. By integrating the improved ETL into the device-fabrication process, we designed QLEDs with the following structure: ITO//double ETL//QDs//CBP//MoO_3//Al. (Figure 4.1) TPBI was identified as a strong candidate for this purpose because of its mobility and its LUMO level, both of which are suitable for inverted QLEDs. [72]

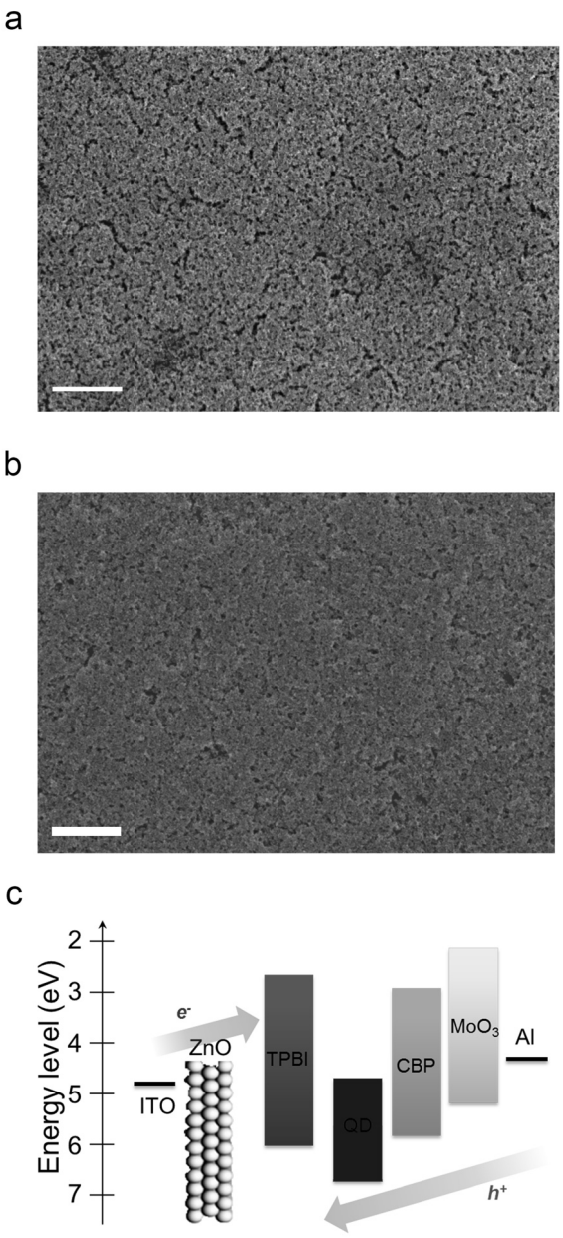

Figure 4.1 Scanning electron microscope (SEM) image of (a) ZnO nanoparticle films and (b) ZnO//TPBI films. (c) energy band diagram of electroluminescent device with blue QDs. (scale bar : 400 nm)

4.2 Characteristics of electroluminescence devices made of a series of double electron transport layers

To investigate the influence of double ETLs on blue QLEDs, the device performance was characterized as a function of TPBI concentration. We fabricated devices with a multilayered structure of ITO//ZnO (40 nm)//TPBI (x nm)//blue QDs (20 nm)//CBP (50 nm)//MoO_3 (10 nm)//Al (100 nm). To investigate the effect of passivation and charge blocking layer, we tested various thicknesses of TPBI in our devices. The TPBI, which was used as an ETL and charge blocking material because of its LUMO level, was spin-coated onto the ZnO layer. CBP (HTL), MoO_3 (hole injection layer), and Al layers were thermally evaporated under 1×10^{-6} Torr. All blue QLEDs showed EL only from the QDs under the full range of current densities (Figure 4.2a), i.e., no emission was observed from the adjacent organic layers (i.e., TPBI and CBP). Figures 4.2b and c show the performance of the double ETL blue QLED devices with different thicknesses of the TPBI layer. From the current density-voltage and luminance-voltage characteristics in Figure 4.2 b, we determined that the current density of the device without TPBI in the low-voltage regime was higher than those of the other devices. This higher current under a low electric field originated from spontaneous electron injection into the QD emissive layer. [35] Increasing the thickness of the TPBI layer slightly increased the driving voltage of the devices. The luminance of the devices with the TPBI layer was higher than that of the only-ZnO device. This increased luminance from the charge blocking layer can be attributed to the adjustment of the spontaneous electron injection *via* the injection barrier between ZnO and TPBI, which also prevents non-radiative recombination in the high-electric field region. Figure 4.2c shows the maximum EQE values: 3.2, 3.4, 3.0, 3.0 and 2.0 % in devices containing 0.25 wt%

to 2.0 wt% TPBI and that without TPBI, respectively. Given the current density value of the maximum EQE of all devices, including TPBI in the ETL alters the hole-electron charge balance in QLEDs. Figure 4.3 shows the influence of the TPBI thickness on the operational stability of the devices. QLEDs containing the TPBI layer exhibited longer lifetimes than those of the control devices.

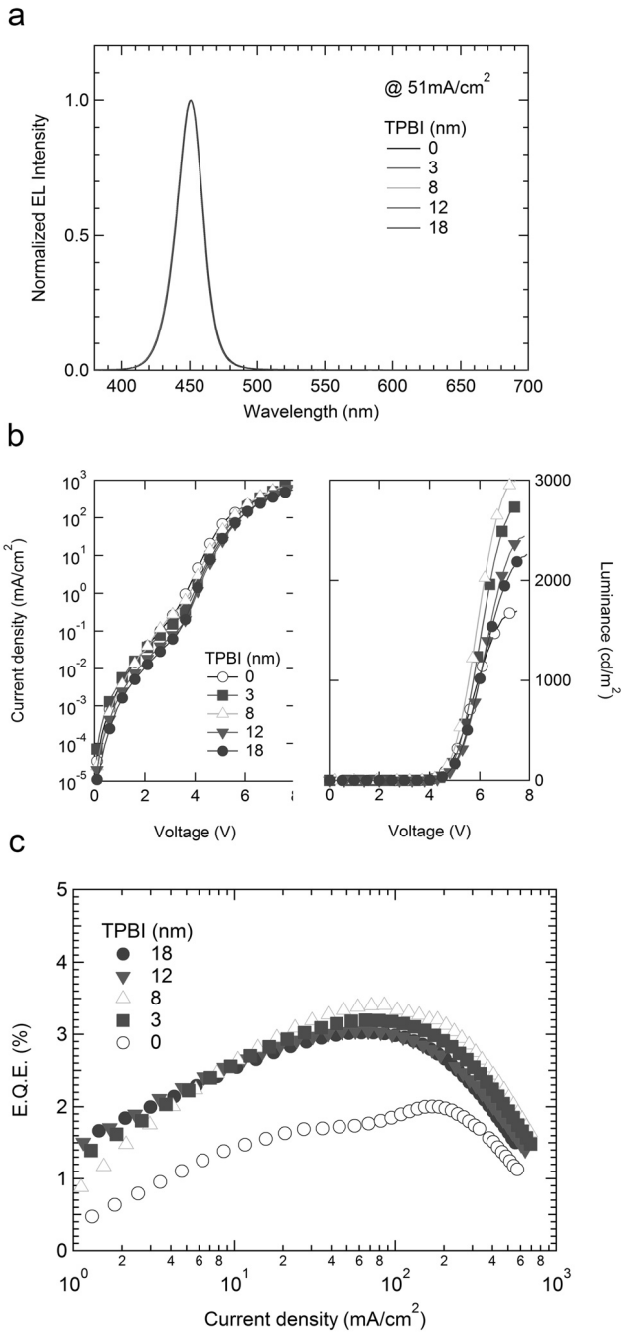

Figure 4.2 (a) Normalized current-dependent electroluminescence spectra (b) current density-voltage-luminance curves and (c) EQE versus current density graphs for QLEDs based on blue QDs of varied TPBI concentration.

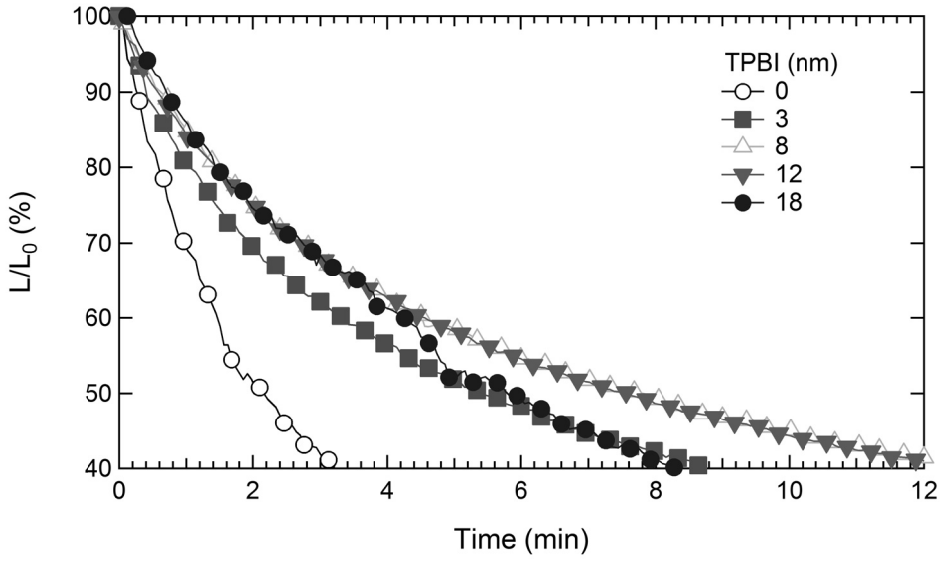

Figure 4.3 Lifetime of QLEDs with varied TPBI concentration

Chapter 5

Cd-free InP QLEDs based on Inverted Device Structures

Although the increasing attention paid to InP QDs is now leading to applied research on InP QLEDs, their full potential remains to be demonstrated. To date, the best InP QLEDs exhibited an EQE of only 0.26 % and a maximum brightness of 700 cd m^{-2}. [73] These values are indeed far inferior to those of QLEDs consisting of alternative materials with relatively lower solution PL QY, such as Si (up to 1.1 % EQE for red emission) [74] or $CuInS_2$ (up to 2,100 cd m^{-2} maximum brightness for orange-red emission). [75] In addition, the color purity of previous InP QLEDs was lower than expected from solution PL spectra and was compromised by the unexpected contribution of broad parasitic emission from adjacent charge transporting layers.

Given that InP QDs possess energy levels comparable to those of alternative emitting materials (VB maximum [VBM]: 3.5 ~ 4 eV and conduction band minimum [CBM]: 5.5 ~ 6 eV) and they have similar device structures, the reason underlying the inferior performance of InP QLEDs remains unknown.

In this part, we demonstrate bright, efficient and environmentally benign green-emitting InP QLEDs with EQEs as high as 3.46 % and brightness as high as 3,900 cd m^{-2}. This breakthrough in device performance was achieved by developing a device architecture that allows for direct charge carrier injection into QDs and the structural formulation of InP/ZnSeS core/shell heterostructured QDs for efficient exciton recombination. The direct charge carrier injection within QDs is assisted by a solution-processed, thin conjugated polyelectrolyte (PFN) layer. The PFN layer essentially acts as an interfacial dipole layer between the ZnO ETL and the QDs, reduces the electron injection barrier into the QDs through the vacuum level shift, and promotes the charge balance within the QDs. On the basis of this tailored device structure, we employ highly efficient green InP QDs with thick composition-gradient ZnSeS multi-shells (PL QE > 07 % with ~ 6 monolayers of ZnSeS alloy layers). The thick ZnSeS composition-gradient multi-shells provide a sufficient potential barrier for the effective confinement of generated excitons within InP core domain away from the surface defect states. Because of the finely tuned device structure and the protection of excitons from quenching by surface defect states, the radiative recombination of electrically generated excitons was considerably enhanced, producing InP QLEDs with high efficiency and brightness.

5.1 Preparation of InP QDs with multiple gradient shells

Green-emitting InP QDs with multiple ZnSeS composition gradient shells were prepared by a modified synthetic procedure developed by J. Lim et al. [26] The composition gradient is such that Se is dominantly located close to the InP cores, and the S content increases along the radial direction of the shell. The presence of Se mitigates compressive lattice strain between the InP core and the ZnS shell phases and facilitates the uniform growth of ZnS shells, thereby enhancing both the PL QE and the stability against various stresses that deteriorate QDs (i.e., heat, UV-irradiation, ligand exchange, and purification). To ensure the uniform growth of highly crystalline ZnSeS composition-gradient shells on top of InP cores, we adopted precursors with low reactivity (i.e., 1-dodecanethiol for S precursors instead of S-trioctylphosphine) and performed the shell growth at an elevated reaction temperature (300 °C) to induce thermodynamic shell growth conditions. The reaction schemes involved multiple shell growth steps for the thick ZnSeS shell to prevent inhomogeneous shell growth or the homogeneous nucleation of ZnSeS particles at high precursor concentrations.

Figure 5.1 presents the characteristics of prepared InP@ZnSeS QDs. We started from the same-sized InP QDs with an average diameter of 1.1 nm (estimated from the first excitonic transition peak) and performed multiple ZnSeS shelling with different compositions and shell thicknesses. Unexpectedly, InP@ZnSeS QDs showed excellent PL QY for the optimized Se content, even with a large shell thickness (Table 5.1): PL QY > 80 % for InP@ZnSeS QDs with a shell thickness of 1.1 nm (Figure 5.1a), > 70 % for InP@ZnSeS with a shell thickness of 1.7 nm (Figure 4.1b), and > 45 % for InP@ZnSeS with a shell thickness of 2.1 nm in the green emission range (λmax: 500 ~ 520 nm, FWHM ~ 50 nm). Compared with

previous InP-based QDs, which exhibit 40 ~ 60 % PL QY for thin ZnS [44] or ZnSe/ZnS shells (thickness below 1 nm) only, [45] our QDs, which were able to produce high PL QY, strongly suggest that the composition-gradient ZnSeS multi-shells effectively mitigate the lattice strain, even for large shell thicknesses. No significant changes were observed in the PL wavelength or the single exciton decay dynamics for the series of InP@ZnSeS QDs with different shell thicknesses, indicating that charge carrier wave functions were effectively confined within an inner shell (1.1 nm) and were not affected by the additional ZnSeS shell layers. The energy off-set between the InP core and ZnSeS shell (CBM offset ~ 0.3 eV, VBM offset ~ 0.8 eV) [26] and the effective mass of charge carriers (m_e = 0.077 and m_h = 0.64 for InP) together suggest that holes are strongly confined within the InP core domain, whereas electrons are delocalized to the ZnSeS shell phase to limited extent (~ 1.1 nm), similarly to the case of CdSe/CdS core/shell heterostructures. [56, 76, 77] Prepared InP@ZnSeS QDs exhibited VBM values of ~ 5.9 eV and CBM values ~ 3.5 eV, as estimated from ultraviolet (UV) photoelectron spectroscopy (UPS) and UV-visible absorption measurements (Figure 5.2 and Table 5.2). We note that the energy level positions of InP@ZnSeS QDs are closer to the vacuum level than those of Cd-based green QDs. [9]

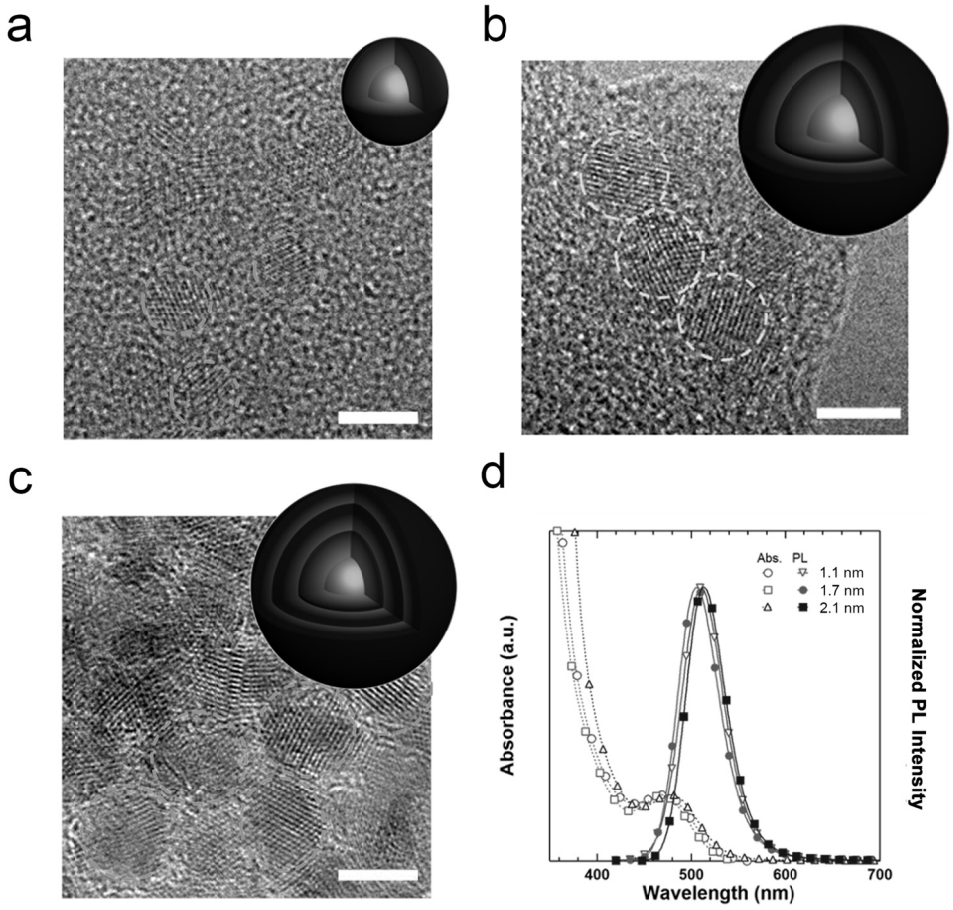

Figure 5.1 Transmission electron microscopy (TEM) image of InP@ZnSeS QDs with (a) 1.1 nm of shell thickness, (b) 1.7 nm of shell thickness (c) 2.1 nm of shell thickness. (Scale bars: 5 nm), and (d) Absorption (open) and photoluminescence (closed) spectra of InP QDs with different shell thickness.

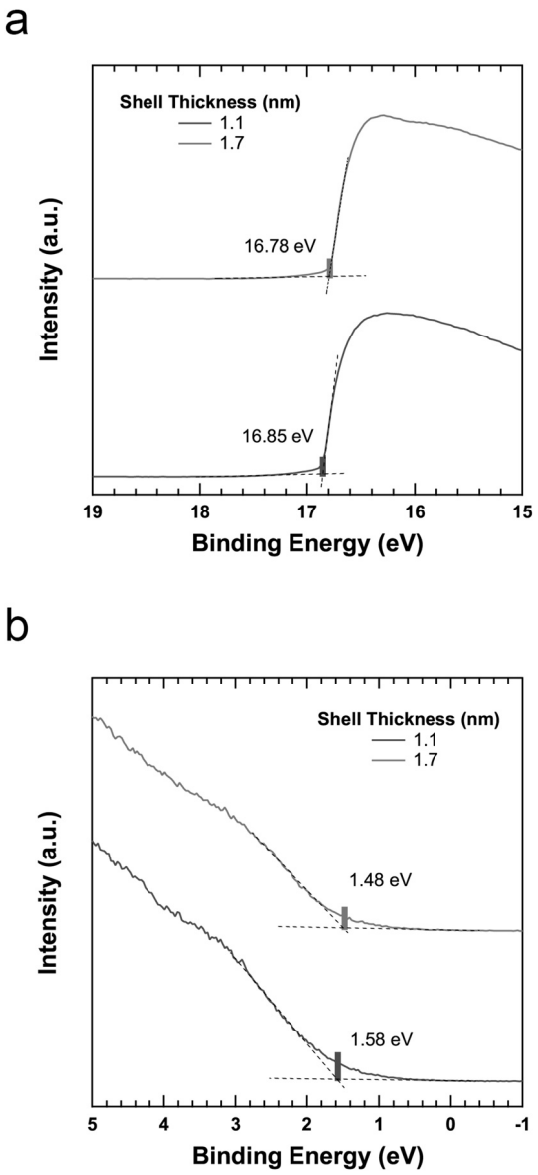

Figure 5.2 (a) High binding energy cut-off region and (b) valence band region (right) in UPS of InP@ZnSeS QDs with 1.1 nm (red) and 1.7 nm (green) shell thickness.

Table 5.1 Atomic contents of InP@ZnSeS QDs

	Shell Thickness		
	0.6 nm (adjacent to InP core)	1.1 nm	1.7 nm
In	7.5 ± 1.5	2.4 ± 0.7	1.7 ± 0.7
P	11 ± 0.9	4.0 ± 0.3	5.9 ± 1.0
Zn	60 ± 1.7	46 ± 0.3	42 ± 4.1
Se	12. ± 2.5	5.8 ± 1.6	2.6 ± 0.9
S	9.3 ± 2.5	42 ± 3.7	45 ± 0.5

Table 5.2 Valence band maximum (VBM), conduction band minimum (CBM), and bandgap (Eg) of InP@ZnSeS QDs

Shell Thickness (nm)	VBM (eV)	CBM (eV)	E_g (eV)
1.1	5.90	3.52	2.38
1.7	5.93	3.54	2.39

5.2 Adopting conjugated polyelectrolyte layer for InP QLEDs

We applied the improved green InP@ZnSeS QDs in QLEDs and used the inverted device structure, in which a transparent ITO electrode serves as a cathode, and Al serves as an anode (Figure 5.3a). This device architecture has recently been utilized in current-driven organic LEDs and QLEDs because it promotes better device stability, [78] easy integration of unit devices with TFT backplanes, [79] and facile selection of hole transporting materials by thermal evaporation. [9] In addition, the inverted device structure with hybrid (organic and inorganic) CTLs is known to be particularly useful for optimizing the carrier transport in QLEDs. [9] The underlying metal oxide ETL facilitates the barrier-less injection of electrons from the cathode (ITO) and also provides mechanical robustness for the deposition of QDs based on solution-processing methods and HTL/anode processed by vacuum evaporation or sputtering methods. In addition, the inverted device structure enables the full utilization of commercially available hole transporting materials with proven electronic properties and stability. In the present study, we adopted ZnO nanoparticle thin films as the ETL and 4,4',4''-tris(N-carbazolyl)-triphenylamine (TCTA) as the HTL. The ZnO nanoparticle layer is highly advantageous for EL devices because of its optical transparency in the visible region (bandgap ~ 3.3 eV) and solution processability at low temperature (< 100 °C). [9] TCTA was chosen as the HTL as a counterpart for the ZnO ETL because its HOMO energy level (5.7 eV) [9] is close to the VBM of InP@ZnSeS QDs (5.9 eV) and its hole mobility is 4×10^{-4} $cm^2V^{-1}s^{-1}$, similar to that of the ZnO ETL.

Unlike the case of QLEDs with II-VI QDs, in which electron injection occurs easily, even without an applied voltage, hole injection requires the assistance of an

electric field.[35] The present InP QLEDs have a higher energetic barrier for electron injection from ZnO into the InP@ZnSeS QDs (~ 0.5 eV) than that for hole injection from TCTA into QDs (0.2 eV) (see Figure 5.3b left). The difference in the injection barriers for electrons and holes will likely lead to asymmetric charge injection and charge imbalance within the QDs (containing excess holes), resulting in non-radiative exciton decay pathways *via* Auger recombination. In addition, such an injection barrier also increases the operational driving voltage (electric field) for QLEDs, thus giving rise to the decrease in the PL QY of the QDs and subsequent operational efficiency loss in devices. [52]

A clear first step for the improvement of device performances was to facilitate the electron injection from ZnO into InP@ZnSeS QDs. For this aspect of the device structure, we introduced a thin conjugated polyelectrolyte layer of PFN at the interface between ZnO and InP@ZnSeS QDs to reduce the electron injection barrier (see Figure 5.3b right). The PFN layer serves as an interfacial dipole layer and is known to achieve a vacuum level shift exceeding 0.5 eV. [80-83] In addition, PFN is poorly soluble in nonpolar solvents (such as hexane or toluene) and enables orthogonal processing to realize multilayered structures (i.e., ZnO nanocrystal layer/PFN thin layer/colloidal QD layer). Thus, on the basis of PFN, we were able to realign the carrier transport levels in the present QLEDs by using the following architecture: a ZnO nanoparticle layer, a PFN thin layer, and an InP QD emission layer were sequentially spin-coated on top of an ITO cathode. TCTA, molybdenum oxide (MoO_3), and Al anode layers were then sequentially evaporated on top of the solution-processed ITO/ZnO/PFN/InP QD layer (Figure 5.3a).

The formation of the interfacial dipole layer and the corresponding vacuum level shift (Δ) at the interface between ZnO and InP@ZnSeS QDs were characterized *via* UPS (Figure 5.4a). The extent of the vacuum level shift of the

ITO/ZnO/PFN thin films could be adjusted up to 0.6 eV by altering the concentration of the PFN solution (see the inset of Figure 5.4a). We note that the extent of the vacuum level shift saturated at 0.6 eV after deposition using 1.5-mg mL^{-1} PFN.

Photovoltaic characterization is a well-known technique for measuring the built-in voltage of the devices and for confirming the effect of the soluble conjugate polyelectrolytes adopted in organic devices. [81, 82, 84] To measure the photovoltaic properties of devices, we prepared complete devices (i.e., ITO/ZnO/PFN/QD/TCTA /MoO_3/Al) and illuminated them at AM 1.5 G (100 $mWcm^{-2}$). As shown in Figure 4.4b, the built-in potential or open-circuit voltage (V_{OC}) was determined by the difference between the CB of ZnO and the VB of the QDs. The V_{OC} increased by approximately 0.2 eV when a PFN layer was included in the InP QLEDs (see Figure 5.4c). These results indicate that the electron injection barrier between ZnO and QD can be significantly decreased by employing PFN layers, thereby improving the charge injection balance in InP QLEDs. Additionally, as shown by the detailed results, their photovoltaic characteristics are quite consistent with those of InP QLEDs. Furthermore, the extent of the energy level shift in UPS data was similar to the V_{OC} shift in the same devices. Thus, we confirmed the dipole effect in the interface between ZnO and InP QD through UPS and photovoltaic measurements.

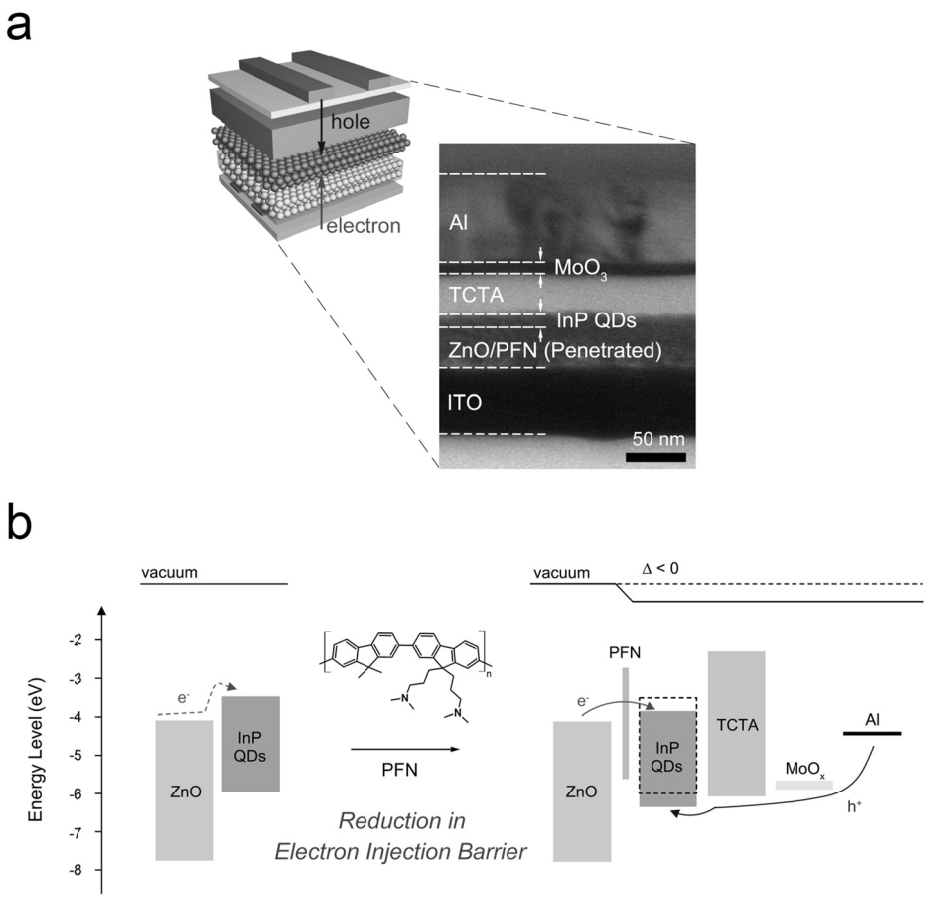

Figure 5.3 (a) A schematic illustration (left) and a cross-sectional TEM image (right) of QLED in inverted device structure, (b) Flat band energy-level diagrams of QLEDs illustrating the reduction in electron injection barrier between ZnO and QDs due to the presence of PFN layer. (Δ: The change in the vacuum level shift)

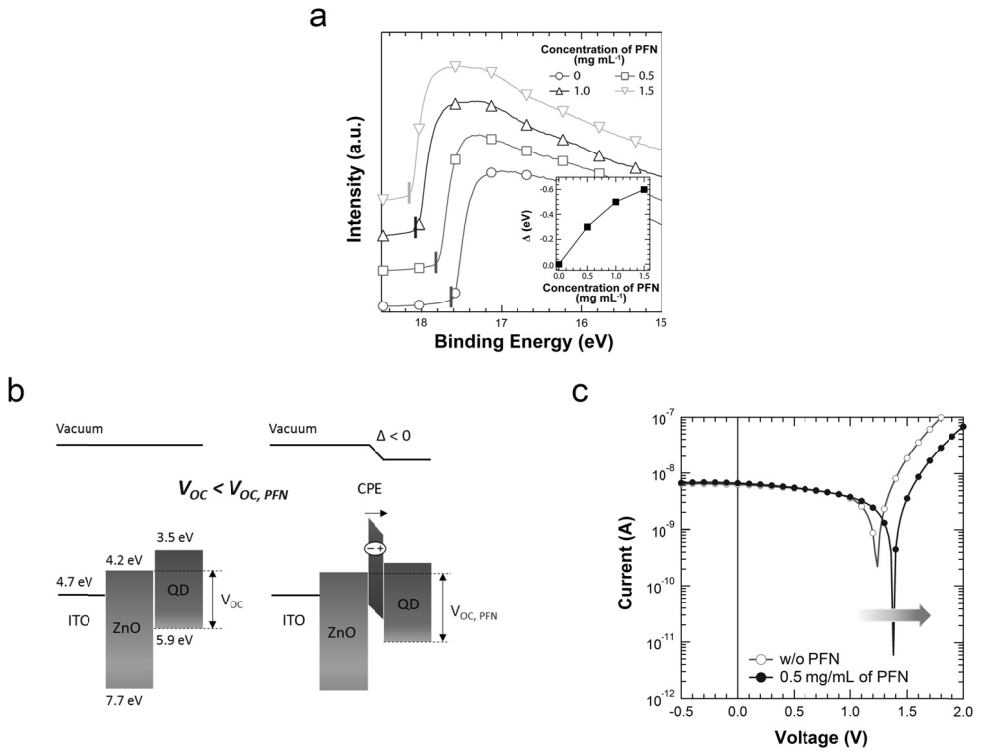

Figure 5.4 (a) Expanded UPS spectra near the binding energy cutoff region of a bare ZnO film and PFN-coated ZnO films on ITO substrates. The UPS spectra of PFN-coated ZnO films are vertically shifted for clarity. (Inset: the change in the vacuum level shift (Δ) vs. PFN concentration), (b) Flat band energy-level diagrams of QLEDs illustrating the reduction in electron injection barrier between ZnO and QDs due to the presence of PFN layer, and (c) Photovoltaic characteristics of QLEDs with (closed) and without (open) PFN layers under AM1.5G illumination.

No significant change in the surface morphology or roughness of ZnO ETLs was observed on PFN-covered ZnO films (Figure 5.5 and Table 5.3), thus leading us to conclude that the difference in the device characteristics can be essentially attributed to the changed electron injection properties between ZnO and InP@ZnSeS QDs resulting from the vacuum level shift (Figures 5.3b and 5.4b) rather than the morphological changes in the ZnO QDs or QD active layers.

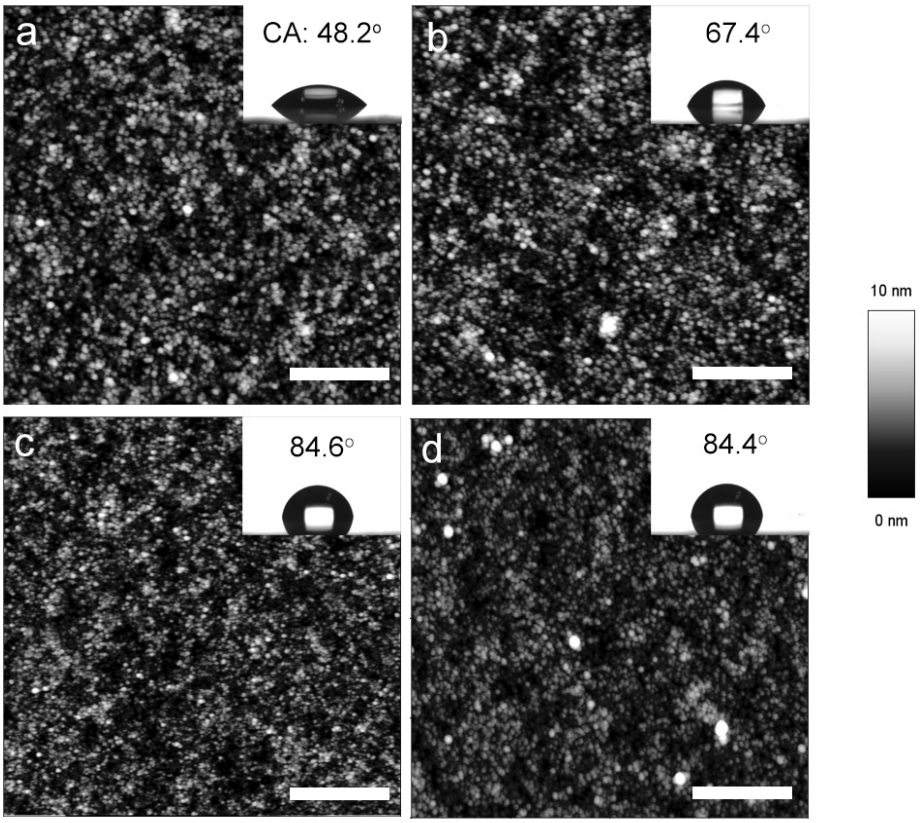

Figure 5.5 AFM height images and water contact angles (inset) of ZnO/PFN thin films prepared with (a) 0; (b) 0.5; (c) 1.0; and (d) 1.5 mg mL^{-1} of PFN concentration (scale bar: 500 nm).

Table 5.3 A summary of root-mean-square roughness and thickness of ZnO/PFN thin films given in Figure 5.5

Concentration of PFN solution (mg mL^{-1})	RMS roughness (nm)	Thickness (nm)
0	1.5	45.2
0.5	1.6	43.1
1.0	2.4	44.5
1.5	1.3	47.5

5.3 Characteristics of green InP QLEDs using PFN layers

To investigate the influence of the extent of the vacuum level shift on the electron injection characteristics, the device performance was characterized as a function of PFN concentration (see Figure 5.6). To fabricate the devices, first, a 20-mg mL^{-1} ZnO solution was spun onto a patterned ITO substrate at 2000 rpm for 60 sec and then baked under N_2 atmosphere at 90 °C for 30 min. The resulting film thickness was 45 nm. Next, 0.5-mg mL^{-1} PFN (purchased from 1-materials Inc.) solution in methanol/acetic acid (acetic acid:methanol = 2 μL:1 mL) was spun onto the ZnO layer and then dried for 30 min under vacuum. Subsequently, a 5-mg mL^{-1} QD dispersion was deposited by spin-casting at 4000 rpm for 30 sec to be equivalent to 2 ~ 3 monolayers of QDs. Finally, TCTA (50 nm), MoO_3 (10 nm), and Al (100 nm) were sequentially evaporated to achieve deposition rates of 0.5–1 Å sec^{-1}, 0.2 Å sec^{-1}, and 3–5 Å sec^{-1}, respectively. For systematic comparison, the other electronic components of the QLEDs were optimized as follows: 2 ~ 3 monolayers for the InP@ZnSeS QD emission layers (1.7-nm shell thickness), 40-nm ZnO nanoparticle layer, 50-nm TCTA, and 10-nm MoOx. The presence of a thin PFN layer (0.5-mg mL^{-1} PFN) facilitated the electron injection from ZnO into InP@ZnSeS QDs, as evidenced by the significant decrease in the turn-on voltage (V_{ON}) from 2.8 V to 2.2 V (see Figure 5.6b) (the reduced turn-on voltage is near the voltage equivalent of the optical bandgap energy) and the increased current density (*J*) and luminance (*L*) as compared to the control device (without PFN) (see Figure 5.6b). Interestingly, further increasing the PFN concentration did not guarantee improved device performance. In fact, higher PFN concentrations had negative effects; despite the reduction in the electron injection barrier; increasing the PFN concentration above 0.5 mg mL^{-1} increased the V_{ON} and decreased *J* and *L*. This trade-off in device

performance can be rationalized on the basis of the competing effects of PFN thickness on the charge carrier injection from ZnO into QDs. A thin PFN layer acts as an interfacial dipole layer, reducing the potential difference between ZnO and InP@ZnSeS QDs *via* the vacuum level shift and facilitating the electron injection from ZnO to QDs across the PFN layer (tunneling process). A thick PFN layer further reduces the potential barriers but simultaneously increases the width of the tunneling barrier (the thickness of the PFN itself), thereby impeding the tunneling of electrons from ZnO into the InP@ZnSeS QD emission layer. The characteristics of QLEDs as a function of PFN deposition concentration are summarized in Table 5.4.

The comprehensive adjustments of the carrier transport layers facilitates electron injection into InP QDs and consequently enhances the charge balance within QDs, as clearly evidenced by the dramatic increase in the device efficiency (Figure 5.6c). Although further increasing the concentration of PFN beyond the optimal value also enhanced EQE in the low-current density regime, the resulting increased resistance caused by the PFN layer lowered the overall EQE level and luminance of devices. The opposing trends of EQE between the devices without PFN and those containing a large amount of PFN (at ~ 10 mA cm^{-2}, 1.0 and 1.5 mg/mL samples in Figure 5.6c) reflected the effect of interfacial resistance on EQE, which effectively blocked the injection of electrons into QDs. The optimized device with the thinnest PFN layer showed enhanced performance, with a maximum EQE of 3.46 % and maximum brightness of 3,900 cd m^{-2}, without parasitic peaks from adjacent carrier transport layers under varied current densities (Figure 5.6d). Moreover, large-area (1.2 cm × 1.2 cm) flexible InP QLEDs with uniform brightness over the entire pixel were demonstrated on the device platform (inset in Figure 5.6d), validating the process capability of PFN layers for practical applications in large-area displays or lighting systems. To the best of our knowledge, the EQE, maximum

brightness, and spectral purity of the present QLED devices are the highest values ever recorded for Cd-free QD-based LEDs emitting visible light.

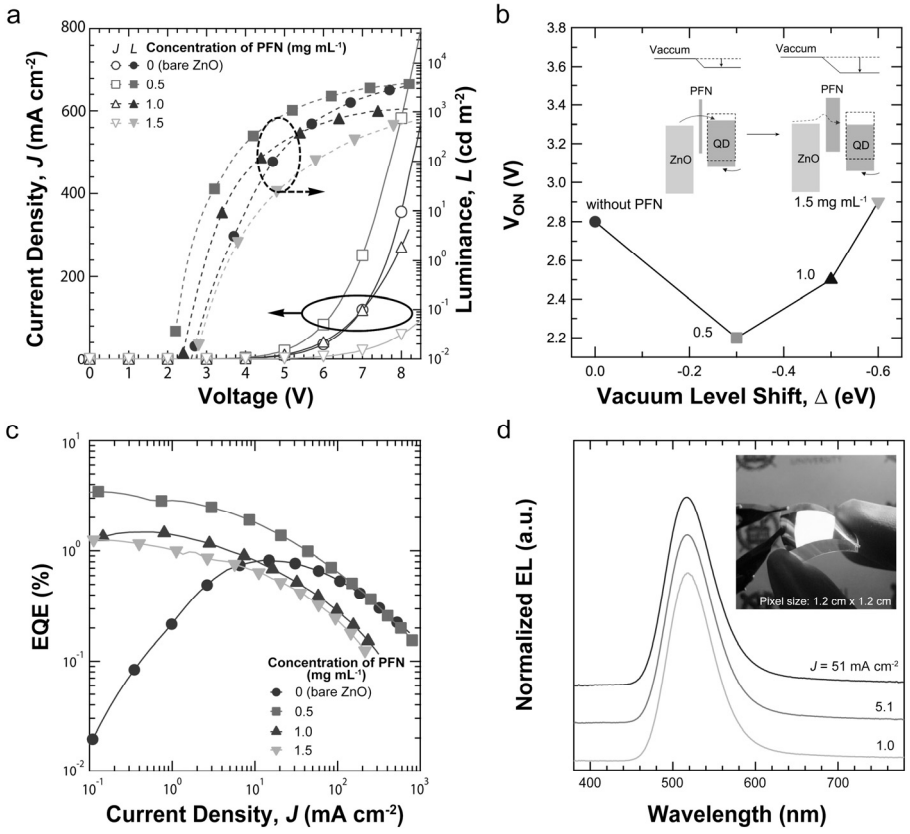

Figure 5.6 (a) Current density (*J*) - voltage (*V*) - luminance (*L*) characteristics, (b) turn-on voltage (V_{ON}), and (c) EQE vs. J characteristics of InP@ZnSeS (1.7 nm of shell thickness) QLEDs prepared with varied PFN concentrations. Vacuum level shift by PFN and corresponding arrangement of energy levels are illustrated as an inset in (b); the increase in the PFN thickness impedes electron tunneling from ZnO to QDs, thus V_{OC} is increased again after optimal condition (green square). (d) Normalized EL spectra of InP@ZnSeS (1.7 nm of shell thickness) QLEDs at different current densities (*J*) (Inset: a photograph of large-area and flexible InP@ZnSeS QLED on a polyethersulphone substrate. pixel size: 1.2 cm × 1.2 cm).

Table 5.4 QLED (1.7 nm of shell thickness) performance as a function of PFN concentration

PL QY (%)	EL λ_{max} /FWHM (nm)	PFN (mg mL^{-1})	V_{on} (V)	Max. EQE (%)	EQE at 100 cd m^{-2} (%)	Max. LE (cd A^{-1})	Max. L (cd m^{-2})
72	518 /64	0	2.8	0.825	0.677	1.53	4,182
		0.5	2.2	3.46	2.90	10.9	3,900
		1	2.5	1.47	1.17	4.6	1,138
		1.5	2.9	1.26	0.811	3.06	801

*Abbreviations and their full meanings: PL QY (photoluminescence quantum yield of QDs), PL (photoluminescence), EL λ_{max} (electroluminescence, at 1 mA/cm^2), V_{on} (turn-on voltage), EQE (external quantum efficiency), LE (luminous efficiency), and L (luminance).

5.4 Effect of shell thickness on based on InP QLED performances.

Appropriate control over the carrier injection and the alignment of energy levels are important requirements for the successful production of efficient QD EL devices and were apparently achieved here. In addition to the previously mentioned needs to improve device performance, the direct injection of carriers and their charge balance are regarded as the key factors for creating efficient EL devices, as clearly demonstrated here. In addition, we found that the shell thickness of InP QDs also contributes to the performance of InP QLEDs. We varied the shell thickness of InP QDs by increasing the thickness of ZnSeS composition gradient shells from 1.1 nm to 2.1 nm (Figure 5.1) and investigated the effects on device performance (Figure 5.7 and Table 5.5). This comparison was possible because of the advanced synthetic method presented above, which prevented the formation of internal defect states in the shell phase while increasing the shell thickness. Surprisingly, InP@ZnSeS QDs with thicker shells clearly showed better device performance in terms of EQE and maximum brightness than those with thinner shells (Figure 5.7 and Table 5.5). Interestingly, the EQEs of QLEDs were determined by both PL QE and shell thickness: among QDs with similar PL QE (t = 1.1 nm and 1.7 nm), thicker shells resulted in better device performance. However, the QDs with poor PL QE and the thickest shell exhibited the worst EQE.

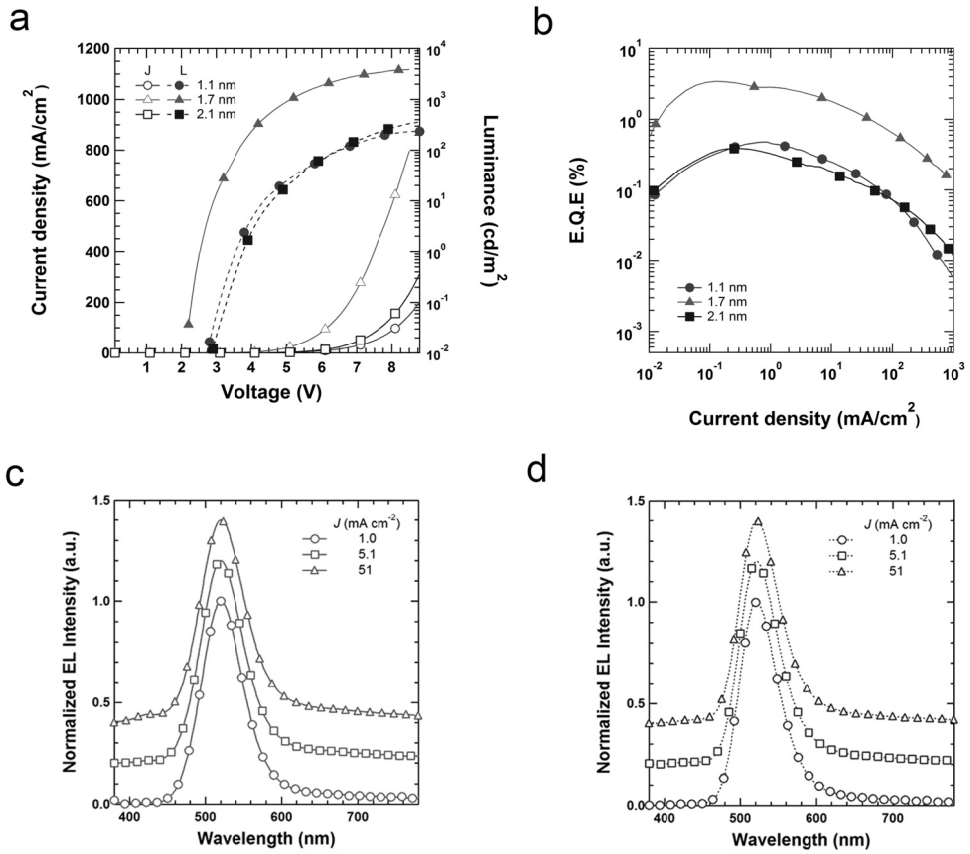

Figure 5.7 (a) *J-V* and *L-V* characteristics, (b) EQE-*J* curves of InP QLEDs comprising of various shell thickness of InP QDs. EL spectra of QLEDs based on InP@ZnSeS QDs with (c) 1.1 nm and (d) 2.1 nm of shell thickness at different current densities.

Table 5.5 InP QLED (1.1 nm and 2.1 nm of shell thickness) performance

t (nm)	PL QY (%)	EL λ_{max} /FWHM (nm)	V_{on} (V)	Max. EQE (%)	EQE at 100 cd m^{-2} (%)	Max. LE (cd A^{-1})	Max. L (cd m^{-2})
1.1	81	520/ 65	2.1	0.480	0.201	1.5	236
2.1	45	521/ 60	2.3	0.387	0.130	1.3	405

* t (shell thickness), PFN concentration (0.5 mg mL^{-1}) in these devices.

The improved EQE resulting from increased shell thickness implies that the excitons in InP QDs are readily affected by the surrounding environment. In core@shell QDs, the shell provides a potential barrier to confine the carriers, thereby governing the extent of exciton delocalization to surface states or electronic coupling between QDs.[85] In terms of dot-to-dot spacing, an increase in the shell thickness reduces the energy/charge transfer between QDs. [86, 87] Given that the InP QDs described here have light electron effective masses (i.e., m_e = 0.077 for InP and 0.13 for CdSe) and small CB offsets between the InP and ZnSeS (below 0.3 eV [26]), the excitons or charge carriers in InP QDs are more likely to delocalize to surface states or the surroundings (i.e., adjacent QDs or CTLs) than those in common CdSe/ZnS QDs. According to the intrinsic electronic properties of InP, three photophysical processes of carriers are responsible for the shell thickness-dependent EQE of QLEDs: (i) electron transfer from QDs to the adjacent metal oxide layer, [88, 89] (ii) electron transfer to surface states,[90] and (iii) ET between QDs. [87, 91] Processes (i) and (ii) are closely related to the charging of QDs, which prevents the radiative recombination of excitons through nonradiative Auger recombination. [34, 90, 92] In addition, ET ((iii)) between QDs reduces the PL QE of QD film, thereby also limiting device performance.

Given the possible carrier dynamics on InP QDs, we presume that the increased shell thickness reduced the EQE-limiting processes during device operation by providing a potential barrier and inter-dot spacing between QDs. The potential barrier reduces the formation of surface-localized carriers and charge transfer to the surroundings and subsequent Auger recombination, and the increased spacing between the InP cores inhibits ET between QDs. More importantly, flooding of the charged carriers during device operation expedites the formation of charged QDs *via* trapped carriers on the surface states, and thicker shells decrease the Auger process

by screening the interaction between excitons and the charge carriers trapped on the QDs. Accordingly, the higher accessibility of charge carriers and excitons and the small spacing between QDs in thin ZnSeS shells (t = 1.1 nm) prevent the efficient radiative recombination of electrically generated excitons in QDs, leading to low EQE. Additionally, the thickest tested InP@ZnSeS QDs shell (t = 2.1 nm) was beneficial for reducing the nonradiative processes mentioned above; however, this material's low PL QE limits EQE during device operation. In the present study, InP@ZnSeS QDs (t = 1.7 nm) appeared to have both a sufficient potential barrier width and a high PL QE, and as a result, they exhibited the best performance.

J-dependent EL spectra of InP@ZnSeS QDs for different shell thickness provided intuitive clues regarding the contribution of the extended ZnSeS shell phase to QLED performance. In the semi-logarithmic plots of the normalized EL spectra (Figure 5.8), three QLED devices based on three different types of QDs showed faint emission tails (contributing less than 10 % to the overall EL spectrum), which were not detectable in solution PL. Interestingly, InP@ZnSeS QDs with a shell thickness of 1.1 nm showed more distinct tails that increased as the current density increased. In contrast, InP@ZnSeS QDs with a shell thickness of 1.7 nm produced significantly reduced tails that were nearly independent of *J*. In contrast, InP@ZnSeS QDs with a shell thickness of 2.1 nm exhibited negligible tails. In general, broad emission below the optical bandgap is surface state emission, which originates from the carrier recombination occurring at surface states. Hence, the evolution of EL emission tails from InP@ZnSeS QDs with a thin shell reflects the increased accessibility of electrically generated excitons to the surface-states; under applied bias, the electric field drags electron wave functions outside and facilitates surface state-mediated recombination. Additionally, at high current density, a large

number of charge carriers can be trapped on the surface states of QDs, thus increasing the probability of surface-state emission.

In this context, we believe that the InP@ZnSeS QDs with a shell thickness of 1.7 nm buffer the delocalization of electrons from the inner part of the QDs caused by the electric field, thereby improving the QE of the QLEDs. Although the shell thickness of 1.1 nm provides a marginal potential barrier and electrons are prone to access surface states, increasing the shell thickness results in a sufficient potential barrier against these processes. Interestingly, the addition of 0.6 nm of shell thickness resulted in a 7-fold enhancement of EQE, which can be attributed to an exponentially decreasing probability of electron wave functions in the potential barrier. In summary, to minimize surface state-mediated exciton decay during device operation, the shell phase must be designed to possess the large band offset and a wide barrier width.

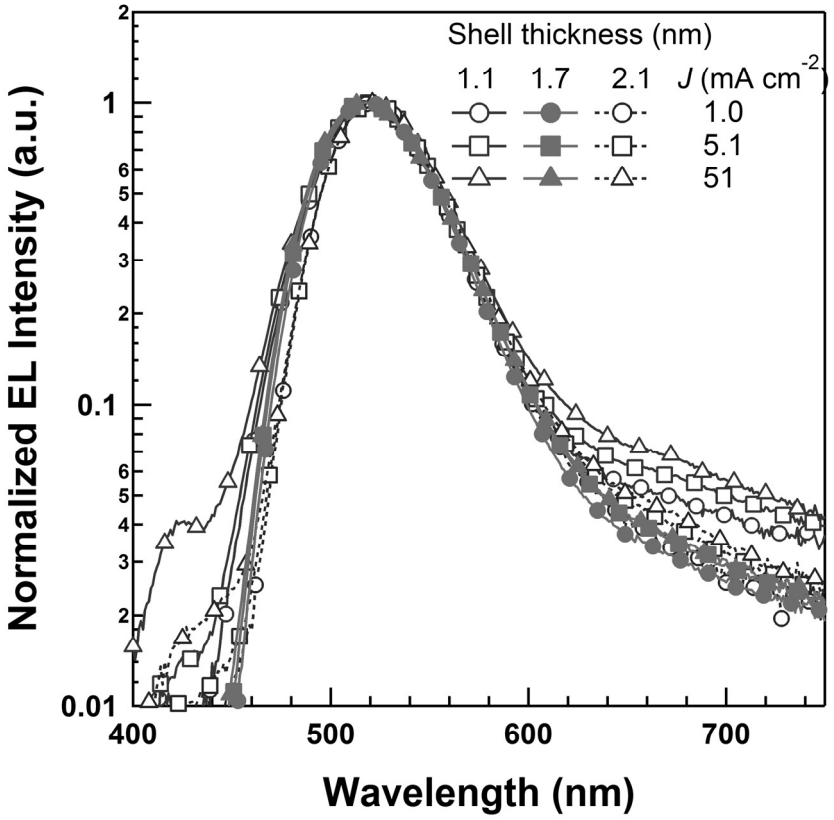

Figure 5.8 Semi-logarithmic normalized EL spectra of InP@ZnSeS QLEDs at different current densities: 1.1 nm (red), 1.7 nm (green) and 2.1 nm (blue) of shell thickness.

5.5 Summary

In summary, we demonstrated environmentally benign, highly efficient, and bright InP@ZnSeS QLEDs based on an advanced synthetic method for InP QDs and tailored device structures. From a practical perspective, the results given here certainly narrow the gap between the device performance of Cd-free QLEDs and the industrial requirements for practical applications. The EQEs of the InP QLEDs in the present study are the highest among the alternative technologies for Cd-free QLEDs that are currently available. More importantly, our research could open up important directions for the structural design of devices and the core@shell formulation of QDs to further improve InP QLEDs. Regarding the device structure, the appropriate choice and optimization of the carrier transport materials were proven to be crucial for InP QLEDs to facilitate the direct injection of carriers. In addition, we demonstrated that a thick ZnSeS heterostructured shell is important to increase the EQEs of QLEDs by protecting the electrically generated excitons from surface states. In forthcoming research, we believe that an in-depth investigation into nonradiative multicarrier decay during device operation and minute engineering of the core@shell heterostructure to minimize such processes will guide us one step further toward the production of high-performance InP QLEDs.

Chapter 6

Conclusion

In this thesis, high-performance colloidal QLEDs were studied from the perspectives of device mechanisms and device structure engineering. We developed and demonstrated highly efficient RGB QLEDs with improved group II-VI QDs and environmentally benign Cd-free QDs.

First, we investigated the influence of the shell thickness of group II-VI type-I heterostructure QDs on QLED performance. To do so, we used a series of CdSe/$_{Zn1-X}Cd_XS$ core/shell type-I QDs with similar optical properties and different shell thickness. This work is the first systematic investigation of QLEDs involving spectroscopic analysis of QD films. From the work presented in this thesis, we suggest that thick-shell QDs exhibit reduced Auger-type decay rates and suppressed ET within QD films. In addition, we observed extraordinary device performance in terms of high efficiency (peak EQE ~ 7.4 %) and record brightness (105,870 cd/m^2).

The operation stability of the devices was discussed, along with improved device performance. Our suggestions not only offer simple results and approaches but also demonstrate a novel structural design of core/shell heterostructure QDs to allow engineering of the optical properties of QD solids and the performance of the corresponding devices; moreover, they provide rational guidelines for the practical use of QLEDs in high-power light sources.

To improve the ETLs, we demonstrated that the efficiency of inverted QLEDs was enhanced by using a double ETL consisting of ZnO nanoparticles and TPBI as organic electron transport materials. TPBI, a soluble organic electron transport material, fills the voids in ZnO nanoparticle films, thereby reducing the leakage current path. As a result, the efficiency of blue QLEDs was considerably increased; in this work, we observed a maximum EQE of 3.4 %.

For highly efficient InP QLEDs, the inverted device structure with a ZnO ETL was adopted because of its numerous advantages in process and integration. However, the large difference in the CB between InP QDs and ZnO impedes efficient electron injection from ZnO to InP QDs. To solve the injection issue, a solution-processable PFN layer was selected as an interfacial dipole layer. Because of the different solubilities of ZnO, PFN, and QDs, stacking the three different layers substantially improved device performance in terms of the maximum EQE (3.46 %) and the maximum luminance (3900 cd/m^2). In our forthcoming research, we believe that an in-depth investigation of nonradiative multicarrier decay during device operation and minute engineering of the core@shell heterostructure to minimize such processes will guide us one step further toward the realization of high-performance InP QLEDs.

In conclusion, this thesis provides a novel approach to increase the efficiency and carrier injection of inverted QLEDs. Furthermore, the physical properties of

QDs were systematically studied to elucidate a method to maximize device performance. In addition, the novel InP QLED structure could be applied to a variety of optoelectronic devices, such as thin-film solar cells, LEDs and transistors.

Bibilography

[1] C. B. Murray, D. J. Norris, M. G. Bawendi, "Synthesis and Characterization of Nearly Monodisperse CdE (E = S, Se, Te) Semiconductor Nanocrystallites" *J. Am. Chem. Soc.* **115**, 8706 (1993)

[2] V. L. Colvin, M. C. Schlamp, A. P. Alivisatos, "Light-emitting diodes made from cadmium selenide nanocrystals and a semiconducting polymer" *Nature* **370**, 354 (1994)

[3] S. Coe, W. K. Woo, M. Bawendi, V. Bulovic, "Electroluminescence from single monolayers of nanocrystals in molecular organic devices" *Nature* **420**, 800 (2002)

[4] P. O. Anikeeva, J. E. Halpert, M. G. Bawendi, V. Bulovic, "Electroluminescence from a mixed red-green-blue colloidal quantum dot monolayer" *Nano Lett.* **7**, 2196 (2007)

[5] B. Dubertret, P. Skourides, D. J. Norris, V. Noireaux, A. H. Brivanlou, A. Libchaber, "In vivo imaging of quantum dots encapsulated in phospholipid micelles" *Science* **298**, 1759 (2002)

[6] D. J. Bharali, D. W. Lucey, H. Jayakumar, H. E. Pudavar, P. N. Prasad, "Folate-receptor-mediated delivery of InP quantum dots for bioimaging using confocal and two-photon microscopy" *J. Am. Chem. Soc.* **127**, 11364 (2005)

[7] A. G. Pattantyus-Abraham, I. J. Kramer, A. R. Barkhouse, X. H. Wang, G. Konstantatos, R. Debnath, L. Levina, I. Raabe, M. K. Nazeeruddin, M. Gratzel, E. H. Sargent, "Depleted-Heterojunction Colloidal Quantum Dot Solar Cells" *ACS Nano* **4**, 3374 (2010)

[8] I. L. Medintz, H. T. Uyeda, E. R. Goldman, H. Mattoussi, "Quantum dot bioconjugates for imaging, labelling and sensing" *Nat. Mater.* **4**, 435 (2005)

[9] J. Kwak, W. K. Bae, D. Lee, I. Park, J. Lim, M. Park, H. Cho, H. Woo, D. Y. Yoon, K. Char, S. Lee, C. Lee, "Bright and Efficient Full-Color Colloidal Quantum Dot Light-Emitting Diodes Using an Inverted Device Structure" *Nano Lett.* **12**, 2362 (2012)

[10] B. S. Mashford, M. Stevenson, Z. Popovic, C. Hamilton, Z. Q. Zhou, C. Breen, J. Steckel, V. Bulovic, M. Bawendi, S. Coe-Sullivan, P. T. Kazlas, "High-efficiency quantum-dot light-emitting devices with enhanced charge injection" *Nat. Photonics* **7**, 407 (2013)

[11] L. Kim, P. O. Anikeeva, S. A. Coe-Sullivan, J. S. Steckel, M. G. Bawendi, V. Bulovic, "Contact Printing of Quantum Dot Light-Emitting Devices" *Nano Lett.* **8**, 4513 (2008)

[12] J. Lim, W. K. Bae, J. Kwak, S. Lee, C. Lee, K. Char, "Perspective on synthesis, device structures, and printing processes for quantum dot displays" *Optical Materials Express* **2**, 594 (2012)

[13] M. C. Schlamp, X. Peng, A. P. Alivisatos, "Improved efficiencies in light emitting diodes made with CdSe(CdS) core/shell type nanocrystals and a semiconducting polymer" *J. Appl. Phys.* **82**, 5837 (1997)

[14] X. Dai, Z. Zhang, Y. Jin, Y. Niu, H. Cao, X. Liang, L. Chen, J. Wang, X. Peng, "Solution-processed, high-performance light-emitting diodes based on quantum dots" *Nature* **515**, 96 (2014)

[15] Y. Yang, Y. Zheng, W. Cao, A. Titov, J. Hyvonen, R. MandersJesse, J. Xue, P. H. Holloway, L. Qian, "High-efficiency light-emitting devices based on quantum dots with tailored nanostructures" *Nat Photon* **9**, 259 (2015)

[16] S. Reineke, F. Lindner, G. Schwartz, N. Seidler, K. Walzer, B. Lussem, K. Leo, "White organic light-emitting diodes with fluorescent tube efficiency" *Nature* **459**, 234 (2009)

[17] J. S. Steckel, J. P. Zimmer, S. Coe-Sullivan, N. E. Stott, V. Bulović, M. G. Bawendi, "Blue Luminescence from (CdS)ZnS Core–Shell Nanocrystals" *Angew. Chem., Int. Ed.* **43**, 2154 (2004)

[18] S. Coe-Sullivan, J. S. Steckel, W. K. Woo, M. G. Bawendi, V. Bulović, "Large-Area Ordered Quantum-Dot Monolayers via Phase Separation During Spin-Casting" *Adv. Funct. Mater.* **15**, 1117 (2005)

[19] Y. Q. Li, A. Rizzo, R. Cingolani, G. Gigli, "Bright White-Light-Emitting Device from Ternary Nanocrystal Composites" *Adv. Mater.* **18**, 2545 (2006)

[20] J. S. Steckel, P. Snee, S. Coe-Sullivan, J. P. Zimmer, J. E. Halpert, P. Anikeeva, L.-A. Kim, V. Bulovic, M. G. Bawendi, "Color-Saturated Green-Emitting QD-LEDs" *Angew. Chem., Int. Ed.* **45**, 5796 (2006)

[21] Y. H. Niu, A. M. Munro, Y. J. Cheng, Y. Q. Tian, M. S. Liu, J. L. Zhao, J. A. Bardecker, I. Jen-La Plante, D. S. Ginger, A. K. Y. Jen, "Improved Performance from Multilayer Quantum Dot Light-Emitting Diodes via Thermal Annealing of the Quantum Dot Layer" *Adv. Mater.* **19**, 3371 (2007)

[22] Z. N. Tan, F. Zhang, T. Zhu, J. Xu, A. Y. Wang, D. Dixon, L. S. Li, Q. Zhang, S. E. Mohney, J. Ruzyllo, "Bright and color-saturated emission from blue light-emitting diodes based on solution-processed colloidal nanocrystal quantum dots" *Nano Lett.* **7**, 3803 (2007)

[23] P. O. Anikeeva, J. E. Halpert, M. G. Bawendi, V. Bulović, "Quantum Dot Light-Emitting Devices with Electroluminescence Tunable over the Entire Visible Spectrum" *Nano Lett.* **9**, 2532 (2009)

[24] K. S. Cho, E. K. Lee, W. J. Joo, E. Jang, T. H. Kim, S. J. Lee, S. J. Kwon, J. Y. Han, B. K. Kim, B. L. Choi, J. M. Kim, "High-performance crosslinked colloidal quantum-dot light-emitting diodes" *Nat. Photonics* **3**, 341 (2009)

[25] B. Wan Ki, K. Jeonghun, L. Jaehoon, L. Donggu, N. Min Ki, C. Kookheon, L. Changhee, L. Seonghoon, "Deep blue light-emitting diodes based on Cd 1− x Zn x S @ ZnS quantum dots" *Nanotechnology* **20**, 075202 (2009)

[26] J. Lim, W. K. Bae, D. Lee, M. K. Nam, J. Jung, C. Lee, K. Char, S. Lee, "InP@ZnSeS, Core@Composition Gradient Shell Quantum Dots with Enhanced Stability" *Chem. Mater.* **23**, 4459 (2011)

[27] K.-H. Lee, J.-H. Lee, W.-S. Song, H. Ko, C. Lee, J.-H. Lee, H. Yang, "Highly Efficient, Color-Pure, Color-Stable Blue Quantum Dot Light-Emitting Devices" *ACS Nano* **7**, 7295 (2013)

[28] J. Lim, M. Park, W. K. Bae, D. Lee, S. Lee, C. Lee, K. Char, "Highly Efficient Cadmium-Free Quantum Dot Light-Emitting Diodes Enabled by the Direct Formation of Excitons within InP@ZnSeS Quantum Dots" *ACS Nano* **7**, 9019 (2013)

[29] W. K. Bae, J. Lim, D. Lee, M. Park, H. Lee, J. Kwak, K. Char, C. Lee, S. Lee, "R/G/B/Natural White Light Thin Colloidal Quantum Dot-Based Light-Emitting Devices" *Adv. Mater.* **26**, 6387 (2014)

[30] K.-H. Lee, J.-H. Lee, H.-D. Kang, B. Park, Y. Kwon, H. Ko, C. Lee, J. Lee, H. Yang, "Over 40 cd/A Efficient Green Quantum Dot Electroluminescent Device Comprising Uniquely Large-Sized Quantum Dots" *ACS Nano* **8**, 4893 (2014)

[31] V. Bulović, P. Tian, P. E. Burrows, M. R. Gokhale, S. R. Forrest, M. E. Thompson, "A surface-emitting vacuum-deposited organic light emitting device" *Appl. Phys. Lett.* **70**, 2954 (1997)

[32] X. Zhou, M. Pfeiffer, J. S. Huang, J. Blochwitz-Nimoth, D. S. Qin, A. Werner, J. Drechsel, B. Maennig, K. Leo, "Low-voltage inverted transparent vacuum deposited organic light-emitting diodes using electrical doping" *Appl. Phys. Lett.* **81**, 922 (2002)

[33] J. W. Stouwdam, R. A. J. Janssen, "Red, green, and blue quantum dot LEDs with solution processable ZnO nanocrystal electron injection layers" *J. Mater. Chem.* **18**, 1889 (2008)

[34] V. Wood, M. J. Panzer, J. E. Halpert, J. M. Caruge, M. G. Bawendi, V. Bulović, "Selection of Metal Oxide Charge Transport Layers for Colloidal Quantum Dot LEDs" *ACS Nano* **3**, 3581 (2009)

[35] W. K. Bae, Y.-S. Park, J. Lim, D. Lee, L. A. Padilha, H. McDaniel, I. Robel, C. Lee, J. M. Pietryga, V. I. Klimov, "Controlling the influence of Auger recombination on the performance of quantum-dot light-emitting diodes" *Nat. Commun.* **4**, 2661 (2013)

[36] H. Nakamura, W. Kato, M. Uehara, K. Nose, T. Omata, S. Otsuka-Yao-Matsuo, M. Miyazaki, H. Maeda, "Tunable Photoluminescence Wavelength of Chalcopyrite CuInS2-Based Semiconductor Nanocrystals Synthesized in a Colloidal System" *Chem. Mater.* **18**, 3330 (2006)

[37] L. Li, T. J. Daou, I. Texier, T. T. Kim Chi, N. Q. Liem, P. Reiss, "Highly Luminescent CuInS2/ZnS Core/Shell Nanocrystals: Cadmium-Free Quantum Dots for In Vivo Imaging" *Chem. Mater.* **21**, 2422 (2009)

[38] J. Zhang, R. Xie, W. Yang, "A Simple Route for Highly Luminescent Quaternary Cu-Zn-In-S Nanocrystal Emitters" *Chem. Mater.* **23**, 3357 (2011)

[39] D. J. Norris, N. Yao, F. T. Charnock, T. A. Kennedy, "High-Quality Manganese-Doped ZnSe Nanocrystals" *Nano Lett.* **1**, 3 (2001)

[40] N. Pradhan, X. Peng, "Efficient and Color-Tunable Mn-Doped ZnSe Nanocrystal Emitters: Control of Optical Performance via Greener Synthetic Chemistry" *J. Am. Chem. Soc.* **129**, 3339 (2007)

[41] D. Chen, R. Viswanatha, G. L. Ong, R. Xie, M. Balasubramaninan, X. Peng, "Temperature Dependence of "Elementary Processes" in Doping Semiconductor Nanocrystals" *J. Am. Chem. Soc.* **131**, 9333 (2009)

[42] R. Xie, X. Peng, "Synthesis of Cu-Doped InP Nanocrystals (d-dots) with ZnSe Diffusion Barrier as Efficient and Color-Tunable NIR Emitters" *J. Am. Chem. Soc.* **131**, 10645 (2009)

[43] R. Xie, D. Battaglia, X. Peng, "Colloidal InP Nanocrystals as Efficient Emitters Covering Blue to Near-Infrared" *J. Am. Chem. Soc.* **129**, 15432 (2007)

[44] L. Li, P. Reiss, "One-pot Synthesis of Highly Luminescent InP/ZnS Nanocrystals without Precursor Injection" *J. Am. Chem. Soc.* **130**, 11588 (2008)

[45] C. Ippen, T. Greco, A. Wedel, "InP/ZnSe/ZnS: A Novel Multishell System for InP Quantum Dots for Improved Luminescence Efficiency

and Its application in a Light-Emitting Device" *Journal of Information Display* **13**, 91 (2012)

[46] S. Kim, T. Kim, M. Kang, S. K. Kwak, T. W. Yoo, L. S. Park, I. Yang, S. Hwang, J. E. Lee, S. K. Kim, S.-W. Kim, "Highly Luminescent InP/GaP/ZnS Nanocrystals and Their Application to White Light-Emitting Diodes" *J. Am. Chem. Soc.* **134**, 3804 (2012)

[47] Y. Zhang, C. Xie, H. Su, J. Liu, S. Pickering, Y. Wang, W. W. Yu, J. Wang, Y. Wang, J.-i. Hahm, N. Dellas, S. E. Mohney, J. Xu, "Employing Heavy Metal-Free Colloidal Quantum Dots in Solution-Processed White Light-Emitting Diodes" *Nano Lett.* **11**, 329 (2011)

[48] J. Kwak, W. K. Bae, M. Zorn, H. Woo, H. Yoon, J. Lim, S. W. Kang, S. Weber, H.-J. Butt, R. Zentel, S. Lee, K. Char, C. Lee, "Characterization of Quantum Dot/Conducting Polymer Hybrid Films and Their Application to Light-Emitting Diodes" *Adv. Mater.* **21**, 5022 (2009)

[49] C. Pacholski, A. Kornowski, H. Weller, "Self-Assembly of ZnO: From Nanodots to Nanorods" *Angew. Chem., Int. Ed.* **41**, 1188 (2002)

[50] S. R. Forrest, D. D. C. Bradley, M. E. Thompson, "Measuring the Efficiency of Organic Light-Emitting Devices" *Adv. Mater.* **15**, 1043 (2003)

[51] D. Bozyigit, O. Yarema, V. Wood, "Origins of Low Quantum Efficiencies in Quantum Dot LEDs" *Adv. Funct. Mater.* **23**, 3024 (2013)

[52] Y. Shirasaki, G. J. Supran, W. A. Tisdale, V. Bulović, "Origin of Efficiency Roll-Off in Colloidal Quantum-Dot Light-Emitting Diodes" *Phy. Rev. Lett.* **110**, 217403 (2013)

[53] W. K. Bae, S. Brovelli, V. I. Klimov, "Spectroscopic insights into the performance of quantum dot light-emitting diodes" *MRS Bull.* **38**, 721 (2013)

[54] B. N. Pal, Y. Ghosh, S. Brovelli, R. Laocharoensuk, V. I. Klimov, J. A. Hollingsworth, H. Htoon, "'Giant' CdSe/CdS Core/Shell Nanocrystal Quantum Dots As Efficient Electroluminescent Materials: Strong Influence of Shell Thickness on Light-Emitting Diode Performance" *Nano Lett.* **12**, 331 (2011)

[55] Y. Chen, J. Vela, H. Htoon, J. L. Casson, D. J. Werder, D. A. Bussian, V. I. Klimov, J. A. Hollingsworth, ""Giant" Multishell CdSe Nanocrystal Quantum Dots with Suppressed Blinking" *J. Am. Chem. Soc.* **130**, 5026 (2008)

[56] F. García-Santamaría, Y. Chen, J. Vela, R. D. Schaller, J. A. Hollingsworth, V. I. Klimov, "Suppressed Auger Recombination in "Giant" Nanocrystals Boosts Optical Gain Performance" *Nano Lett.* **9**, 3482 (2009)

[57] I. Robel, R. Gresback, U. Kortshagen, R. D. Schaller, V. I. Klimov, "Universal Size-Dependent Trend in Auger Recombination in Direct-Gap and Indirect-Gap Semiconductor Nanocrystals" *Phys. Rev. Lett.* **102**, 177404 (2009)

[58] Y. S. Park, A. V. Malko, J. Vela, Y. Chen, Y. Ghosh, F. García-Santamaría, J. A. Hollingsworth, V. I. Klimov, H. Htoon, "Near-Unity Quantum Yields of Biexciton Emission from CdSe/CdS Nanocrystals Measured Using Single-Particle Spectroscopy" *Phys. Rev. Lett.* **106**, 187401 (2011)

[59] G. E. Cragg, A. L. Efros, "Suppression of Auger Processes in Confined Structures" *Nano Lett.* **10**, 313 (2009)

[60] Y.-S. Park, W. K. Bae, L. A. Padilha, J. M. Pietryga, V. I. Klimov, "Effect of the Core/Shell Interface on Auger Recombination Evaluated by Single-Quantum-Dot Spectroscopy" *Nano Lett.* **14**, 396 (2014)

[61] S. Jun, E. Jang, "Bright and Stable Alloy Core/Multishell Quantum Dots" *Angew. Chem. Int. Ed.* **52**, 679 (2013)

[62] J.-C. Wu, J. Zheng, C. L. Zacherl, P. Wu, Z.-K. Liu, R. Xu, "Hybrid Functionals Study of Band Bowing, Band Edges and Electronic Structures of Cd1−xZnxS Solid Solution" *J. Phys. Chem. C* **115**, 19741 (2011)

[63] G. M. Akselrod, F. Prins, L. V. Poulikakos, E. M. Y. Lee, M. C. Weidman, A. J. Mork, A. P. Willard, V. Bulović, W. A. Tisdale, "Subdiffusive Exciton Transport in Quantum Dot Solids" *Nano Lett.* **14**, 3556 (2014)

[64] P. P. Jha, P. Guyot-Sionnest, "Electrochemical Switching of the Photoluminescence of Single Quantum Dots" *J. Phys. Chem. C* **114**, 21138 (2010)

[65] E. Dekel, D. V. Regelman, D. Gershoni, E. Ehrenfreund, W. V. Schoenfeld, P. M. Petroff, "Cascade evolution and radiative recombination of quantum dot multiexcitons studied by time-resolved spectroscopy" *Phys. Rev. B* **62**, 11038 (2000)

[66] H. Fukagawa, T. Shimizu, H. Hanashima, Y. Osada, M. Suzuki, H. Fujikake, "Highly Efficient and Stable Red Phosphorescent Organic Light-Emitting Diodes Using Platinum Complexes" *Adv. Mater.* **24**, 5099 (2012)

[67] W. Qin, H. Liu, P. Guyot-Sionnest, "Small Bright Charged Colloidal Quantum Dots" *ACS Nano* **8**, 283 (2014)

[68] N. Oh, S. Nam, Y. Zhai, K. Deshpande, P. Trefonas, M. Shim, "Double-heterojunction nanorods" *Nat. Commun.* **5**, (2014)

[69] N. Sekine, C.-H. Chou, W. L. Kwan, Y. Yang, "ZnO nano-ridge structure and its application in inverted polymer solar cell" *Organic Electronics* **10**, 1473 (2009)

[70] S. Shao, K. Zheng, K. Zidek, P. Chabera, T. Pullerits, F. Zhang, "Optimizing ZnO nanoparticle surface for bulk heterojunction hybrid solar cells" *Sol. Energy Mater. Sol. Cells* **118**, 43 (2013)

[71] M. Thambidurai, J. Y. Kim, Y. Ko, H.-j. Song, H. Shin, J. Song, Y. Lee, N. Muthukumarasamy, D. Velauthapillai, C. Lee, "High-efficiency inverted organic solar cells with polyethylene oxide-modified Zn-doped TiO2 as an interfacial electron transport layer" *Nanoscale* **6**, 8585 (2014)

[72] W.-Y. Hung, T.-H. Ke, Y.-T. Lin, C.-C. Wu, T.-H. Hung, T.-C. Chao, K.-T. Wong, C.-I. Wu, "Employing ambipolar oligofluorene as the charge-generation layer in time-of-flight mobility measurements of organic thin films" *Appl. Phys. Lett.* **88**, 064102 (2006)

[73] X. Yang, Y. Divayana, D. Zhao, K. Swee Leck, F. Lu, S. Tiam Tan, A. Putu Abiyasa, Y. Zhao, H. Volkan Demir, X. Wei Sun, "A bright cadmium-free, hybrid organic/quantum dot white light-emitting diode" *Appl. Phys. Lett.* **101**, 233110 (2012)

[74] F. Maier-Flaig, J. Rinck, M. Stephan, T. Bocksrocker, M. Bruns, C. Kübel, A. K. Powell, G. A. Ozin, U. Lemmer, "Multicolor Silicon Light-Emitting Diodes (SiLEDs)" *Nano Lett.* **13**, 475 (2013)

[75] B. Chen, H. Zhong, W. Zhang, Z. a. Tan, Y. Li, C. Yu, T. Zhai, Y. Bando, S. Yang, B. Zou, "Highly Emissive and Color-Tunable CuInS2-Based Colloidal Semiconductor Nanocrystals: Off-Stoichiometry Effects and Improved Electroluminescence Performance" *Adv. Funct. Mater.* **22**, 2081 (2012)

[76] B. Mahler, P. Spinicelli, S. Buil, X. Quelin, J.-P. Hermier, B. Dubertret, "Towards non-blinking colloidal quantum dots" *Nat. Mater.* **7**, 659 (2008)

[77] W. K. Bae, L. A. Padilha, Y.-S. Park, H. McDaniel, I. Robel, J. M. Pietryga, V. I. Klimov, "Controlled Alloying of the Core–Shell Interface in CdSe/CdS Quantum Dots for Suppression of Auger Recombination" *ACS Nano* **7**, 3411 (2013)

[78] Z. He, C. Zhong, S. Su, M. Xu, H. Wu, Y. Cao, "Enhanced power-conversion efficiency in polymer solar cells using an inverted device structure" *Nat Photon* **6**, 591 (2012)

[79] H. Lee, I. Park, J. Kwak, D. Y. Yoon, C. Lee, "Improvement of electron injection in inverted bottom-emission blue phosphorescent organic light emitting diodes using zinc oxide nanoparticles" *Appl. Phys. Lett.* **96**, 153306 (2010)

[80] F. Huang, H. Wu, D. Wang, W. Yang, Y. Cao, "Novel Electroluminescent Conjugated Polyelectrolytes Based on Polyfluorene" *Chem. Mater.* **16**, 708 (2004)

[81] H. Wu, F. Huang, Y. Mo, W. Yang, D. Wang, J. Peng, Y. Cao, "Efficient Electron Injection from a Bilayer Cathode Consisting of Aluminum and Alcohol-/Water-Soluble Conjugated Polymers" *Adv. Mater.* **16**, 1826 (2004)

[82] H. Wu, F. Huang, J. Peng, Y. Cao, "High-efficiency electron injection cathode of Au for polymer light-emitting devices" *Organic Electronics* **6**, 118 (2005)

[83] X. Guan, K. Zhang, F. Huang, G. C. Bazan, Y. Cao, "Amino N-Oxide Functionalized Conjugated Polymers and their Amino-Functionalized Precursors: New Cathode Interlayers for High-Performance Optoelectronic Devices" *Adv. Funct. Mater.* **22**, 2846 (2012)

[84] C. Duan, L. Wang, K. Zhang, X. Guan, F. Huang, "Conjugated Zwitterionic Polyelectrolytes and Their Neutral Precursor as Electron Injection Layer for High-Performance Polymer Light-Emitting Diodes" *Adv. Mater.* **23**, 1665 (2011)

[85] M. C. Beard, G. M. Turner, J. E. Murphy, O. I. Micic, M. C. Hanna, A. J. Nozik, C. A. Schmuttenmaer, "Electronic Coupling in InP Nanoparticle Arrays" *Nano Lett.* **3**, 1695 (2003)

[86] O. I. Mićić, K. M. Jones, A. Cahill, A. J. Nozik, "Optical, Electronic, and Structural Properties of Uncoupled and Close-Packed Arrays of InP Quantum Dots" *J. Phys. Chem. B* **102**, 9791 (1998)

[87] S. A. Crooker, J. A. Hollingsworth, S. Tretiak, V. I. Klimov, "Spectrally Resolved Dynamics of Energy Transfer in Quantum-Dot Assemblies: Towards Engineered Energy Flows in Artificial Materials" *Phys. Rev. Lett.* **89**, 186802 (2002)

[88] K. Tvrdy, P. A. Frantsuzov, P. V. Kamat, "Photoinduced electron transfer from semiconductor quantum dots to metal oxide nanoparticles" *Proceedings of the National Academy of Sciences* **108**, 29 (2011)

[89] N. Song, H. Zhu, Z. Liu, Z. Huang, D. Wu, T. Lian, "Unraveling the Exciton Quenching Mechanism of Quantum Dots on Antimony-Doped SnO2 Films by Transient Absorption and Single Dot Fluorescence Spectroscopy" *ACS Nano* **7**, 1599 (2013)

[90] M. Kuno, D. P. Fromm, H. F. Hamann, A. Gallagher, D. J. Nesbitt, "“On”/“off” fluorescence intermittency of single semiconductor quantum dots" *The Journal of Chemical Physics* **115**, 1028 (2001)

[91] C. R. Kagan, C. B. Murray, M. Nirmal, M. G. Bawendi, "Electronic Energy Transfer in CdSe Quantum Dot Solids" *Phys. Rev. Lett.* **76**, 1517 (1996)

[92] U. Banin, M. Bruchez, A. P. Alivisatos, T. Ha, S. Weiss, D. S. Chemla, "Evidence for a thermal contribution to emission intermittency in single CdSe/CdS core/shell nanocrystals" *The Journal of Chemical Physics* **110**, 1195 (1999)

Publication

[1] International Journals

1. J.Y. Kim, S. Noh, Y. M. Nam, J. Y. Kim, J. Roh, **M. Park**, J. J. Amsden, D. Y. Yoon, C. Lee, and W. H. Jo "Effect of Nanoscale SubPc Interfacial Layer on the Performance of Inverted Polymer Solar Cells Based on P3HT/PC71BM", *ACS Appl. Mater. Interfaces,* **3** (11), 4279–4285 (2011).

2. J. Kwak, W. K. Bae, D. Lee, I. Park, J. Lim, **M. Park**, H. Cho, H. Woo, Do Y. Yoon, K. Char, S. Lee, and C. Lee "Bright and Efficient Colloidal Quantum Dot based Light- Emitting Diodes with inverted structure" *Nano Lett.*, **12** (5), 2362–2366 (2012).

3. J. Kwak, Y. Lyu, S. Noh, H. Lee, **M. Park**, B. Choi, K. Char and C. Lee "Hole transport materials with high glass transition temperatures for highly stable organic light-emitting diodes", *Thin Solid Films* **520** (24), 7157–7163 (2012).

4. L. zur Borg, D. Lee, J. Lim, W. K. Bae, **M. Park**, S. Lee, C. Lee, K. Char and R. Zentel "The effect of band gap alignment on the hole transport from semiconducting block copolymers to quantum dots", *J. Mater. Chem. C* **1** (9),

1722–1726 (2013).

5. H. Lee, C.-M. Kang, **M. Park,** J. Kwak and C. Lee "Improved Efficiency of Inverted Organic Light-Emitting Diodes Using Tin Dioxide Nanoparticles as an Electron Injection Layer", *ACS Appl. Mater. Interfaces* **5** (6), 1977–1981 (2013).

6. J. Park, J. Ho, H. Yun, **M. Park**, J. H. Lee, M. Seo, E. Campbell, C. Lee, S. Pyo and S. Lee "Direct Top-Down Fabrication of Nanoscale Electrodes for Organic Semiconductors Using Fluoropolymer Resists", *Appl. Phys. A*, **111** (4), 1051–1056 (2013).

7. J. Lim*, **M. Park***, W. K. Bae, D. Lee, S. Lee, C. Lee, and K. Char "Highly Efficient Cadmium-Free Quantum Dot Light Emitting Diodes Enabled by the Direct Formation of Excitons within InP@ZnSeS Quantum Dots", *ACS Nano*, **7** (10), 9019–9026 (2013). **(*:co-first)**

8. A. Breivogel, **M. Park**, D. Lee, S. Klassen, A. Kuhnle, C. Lee, K Char and K. Heinze "Push-Pull Design of Bis(tridentate) Ruthenium(II) Polypyridine Chromophores as Deep Red Light Emitters in Light-Emitting Electrochemical Cells", *Eur. J. Inorg. Chem.,* **2014** (2), 288–295 (2014).

9. J. Lim, D. Lee, **M. Park**, J. Song, M. S. Kang, S. Lee, C. Lee, and K. Char "Modular Fabrication of Hybrid Bulk Heterojunction Solar Cells Based on Breakwater-like CdSe Tetrapod Nanocrystal Network Infused with P3HT", *J. Phys. Chem. C,* **118** (8), 3942–3952 (2014)

10. C.-M, Kang, H. Cho, **M. Park**, J. Roh and C. Lee "Effects of Insertion of Hole Injection Layers on Pentacene Rectifying Diodes", *J. Nanosci. Nanotechnol.* **14**

(7), 5301–5303 (2014)

11. W. K. Bae, J. Lim, D. Lee, **M. Park**, H. Lee, J. Kwak, K. Char, C. Lee and S. Lee "R/G/B Natural White Light Thin Colloidal Quantum Dot Based Light-Emitting Devices", *Adv. Mater.* **26** (37), 6387–6393 (2014).

12. J. Lim*, B. G. Jeong*, **M. Park***, J. K. Kim, J. M. Pietryga, Y.-S. Park, V. I. Klimov, C. Lee, D. C. Lee and W. K. Bae "Influence of Shell Thickness on the Performance of Light-Emitting Devices Based on CdSe/$Zn_{1-X}Cd_XS$ Core/Shell Heterostructured Quantum Dots", *Adv. Mater.* **26** (47), 8034–8040 (2014). **(*:co-first)**.

13. **M. Park***, S.-H. Jung*, J. Lim, D.-Y. Kim, H.-J. Kim, S. Lee, H. Jung, S. Lee, C. Lee, J.-K Lee "Semiconductor Nanocrystals in Fluorous Liquids for the Construction of Light-Emitting Diodes", *J. Mater. Chem. C* **3** (12), 2759–2762 (2015). **(*:co-first).**

14. H.-J. Park, H. Jung, S.-H. Kim, **M. Park**, J.-H. Kim, J. Son, B. J. Jung, D.-H. Hwang, C. Lee, J.-K. Lee, J. G. Yoon, S. Y. Yoon "Fluorous solvent-soluble imaging materials containing anthracene moieties", *J. Polym. Sci. Pol. Chem.* **53** (10), 1252–1259 (2015).

15. H. Cho, J. Kwak, J. Lim, **M. Park**, D. Lee, W. K. Bae, Y. S. Kim, K. Char, S. Lee and C. Lee "Soft Contact Transplanted Nanocrystal Quantum Dots for Light-Emitting Diodes: Effect of Surface Energy on Device Performance", *ACS Appl. Mater. Interfaces* **7** (20), 10828–10833 (2015).

16. J. Kwak*, J. Lim*, **M. Park***, S. Lee, K. Char and C. Lee "High-power genuine ultraviolet light-emitting diodes based on colloidal nanocrystal

quantum dots", *Nano Lett.* **15** (6), 3793–3799 (2015). **(*:co-first)**.

17. J. Song, J. Lim, D. Lee, M. Thambidurai, J. Y. Kim, **M. Park**, H.-J song, S. Lee, K. Char, C. Lee "Nanostructured Electron-Selective Interlayer for Efficient Inverted Organic Solar Cells", *ACS Appl. Mater. Interfaces* **7** (33) 18460–18466 (2015).

18. D. Lee, J. Lim, **M.Park**, J. Y. Kim, J. Song, J. Kwak, S. Lee, K. Char, C. Lee "Influence of Sequential Ligand Exchange and Elimination on the Performance of P3HT:CdSe Quantum Dot Hybrid Solar Cells", *Nanotechnology*, **26** (46) 465401-1–465401-9 (2015)

[2] International Conferences

1. **M. Park**, H. Cho, H. Lee, D. Lee, J. Lim, K. Char, S. Lee and C. Lee "Efficient red, green, and blue QD-LEDs fabricated with the QD transplanting process on a common hole-transport layer", 50th SID International Symposium, Seminar & Exhibition, Boston, United States (2012).

2. **M. Park**, D. Lee, J. Lim, J. H. Seo, J. Kwak, K. Char, S. Lee and C. Lee "Improved Performance of Quantum Dot Light Emitting Diodes by Using Double Electron Transport Layers of Metal Oxides" 2013 MRS Spring Meeting & Exhibit, San Francisco, California, United States (2013).

3. **M. Park**, J. Lim, S. Lee, K. Char and C. Lee "Demonstration of Cd-free Quantum Dot Light-Emitting Diodes with Inverted Structure", 8th German-Korean Polymer Symposium, Hamburg, Germany (2013).

4. **M. Park**, J. Lim, W. K. Bae, J. Kwak, S. Lee, K. Char and C. Lee "Highly

Efficient InP@ZnSeS Quantum Dot Light Emitting Diodes by Enhancing Carrier Injection", 8th International Conference on Quantum Dots (QD 2014), Pisa, Italy (2014).

5. **M. Park**, J. Lim, Y. Kwon, H. Jung, J. Kwak, K. Char, S. Lee and C. Lee "Improved Performance of Quantum Dot Light Emitting Diodes by Using Charge Blocking Layer", 52nd SID International Symposium, Seminar & Exhibition(Display Week 2014), San Diego, United States (2014).

6. **M. Park**, S.-H. Jung, J. Lim, H. Jung, S. Lee, J.-K. Lee, C. Lee "Colloidal Quantum Dots in Fluorous Solvents for the Construction of Light-Emitting Diodes", 2015 MRS Spring Meeting & Exhibit, San Francisco, United States (2015).

7. **M. Park,** S-H. Jung, J. Lim, H. Jung, S. Lee, J.-K. Lee, C. Lee "Novel Device Architecture of Quantum Dot Light-Emitting Diodes Employing Orthogonal Process", The 15th International Meeting on Information Display (IMID), Daegu, Korea (2015).

8. **M. Park**, H. Jung, B. G. Jeong, W. K. Bae, C. Lee "Improved Performance of Quantum Dot Light-Emitting Diodes by Using Mixed Electron Transport Layer of Organic Molecules and ZnO Nanoparticles", 13th European Conference on Molecular Electronics, Strasbourg, France (2015).

한글 초록

반도체 나노입자 혹은 양자점은 형태, 크기 및 화학적 조성을 변화시킴으로써 우수한 광학적, 전기적 특성을 제어할 수 있다는 장점을 가지고 있다. 따라서 반도체 나노입자를 전기발광 다이오드, 태양전지, 광촉매 등 빛과 전자의 효율적인 상호변환이 요구되는 광전자소자의 차세대 소재로 적용하고자 하는 연구가 융합적으로 지속되고 있다. 하지만, 성공적인 광전자소자를 제작하기 위해서는, 나노입자의 구조에 대한 이해뿐만이 아니라, 이를 집약시킨 최적의 소자구조 및 제작공정에 대한 포괄적인 고려가 필요하다. 본 학위 논문에서는 고효율의 양자점 발광 다이오드를 제작하기 위해 효율이 떨어지는 원인은 광물리학적으로 분석을 하고, 전하주입장벽 감소를 통한 카드뮴이 없는 고효율 친환경 양자점 발광 다이오드 제작, 그리고 이중 전자수송층 도입을 통한 양자점 발광 다이오드 구동안정성 향상에 대한 연구를 논의하였다.

첫째로 높은 휘도에서의 양자점 발광 다이오드 발광효율 감소의 원인 규명 및 해결에 대해 연구하였다. 인접한 양자점간 energy transfer(ET)로 의해 발생하는 nonradiative Auger recombination 이 양자점 발광 다이오드 특성에 어떤 영향을 주는지 규명하기 위해, 양자점의 쉘 두께를 변화시켜 양자점 간의 거리에 따른 발광 다이오드 특성을 파악하였다. 이러한 원인을 파악하기 위해 광물리학적 분석을 진행하였다. 그 결과, 용액 상태의 양자점 PL 효율과 엑시톤 수명은 양자점의 껍질 크기에 상관없이 동일하지만, 소자 내의 양자점 PL 효율과 엑시톤 수명은 껍질 크기가 클수록 크다는 것을 알 수 있었다. 이러한 이유는 양자점의 크기가 커지면서 인접한 양자점 간의 ET 가 억제되고 양자점의 음전하 충전을 감소시키기 때문이다. 박막에서의 ET 는 발광 다이오드 효율 감소의 주된 원인인데, ET 시간과 양자점 간

거리에 대한 특성 분석을 해보니, 양자점간 거리가 13nm 일때까지는 ET 시간이 거리의 6 승에 비례하고 그 이상에서는 거리의 2 승에 비례했다. 이는 거리가 가까울 때는 Förster resonance ET(FRET)을 통해 ET 가 일어나고 거리가 멀어지면 reabsorption-and-emission 에 의해 ET 가 일어난다는 것을 의미한다. 이러한 결과를 바탕으로 양자점 크기에 따른 발광 다이오드를 제작하였다. 크기가 클수록 외부양자효율과 휘도가 증가하였고, 가장 큰 8.3 nm 크기의 양자점 발광 다이오드는 기존에 발표된 휘도 중에 최고인 100,000 cd/m^2 이상의 휘도를 기록했다. 이로써 광물리학적 분석 결과와 소자의 특성이 일치한다는 것을 알게 되었고, 소자의 효율 감소는 ET 에 의한 nonradiative Auger recombination 이 주된 원인임을 밝혔으며, 양자점 쉘의 크기를 증가시킴으로써 소자 효율을 증가시킬 수 있었다. 또한 소자의 수명에 대한 연구도 진행하였는데, 양자점 발광 다이오드의 초기 수명 감소의 큰 원인은 양자점의 쇠퇴인데, 양자점의 크기가 크면 이 정도도 줄어드는 것을 확인할 수 있었다. 따라서 양자점의 쉘이 두꺼울수록 소자의 효율과 구동 안정성이 증가하는 결과를 얻었다.

둘째로, 역구조 양자점 발광 다이오드는 많은 장점을 가지고 있지만, 전자 수송층으로 이용되는 금속산화물 나노입자는 다공성의 특성을 보일 수 있어, 누설 전류의 원인이 될 수 있고 이는 발광 다이오드의 효율 감소를 야기시킨다. 이를 개선하기 위해 양자점과 금속산화물 전자수송층 사이에 직교성을 이용해 유기 전하 수송층을 용액공정으로 도포하였다. 이러한 이중 전자 수송층은 누설 전류 경로를 막고 양자점의 음전하 충전을 억제하여 발광 다이오드의 외부양자효율과 구동 수명을 향상시켰다. 그리고 주사형 전자현미경(SEM)을 이용하여 전자 수송층 표면을 관찰한 결과, 금속산화물/유기전자수송층 형태의 이중 전자수송층은 핀홀을 덮는 효과가 있음을 확인했다.

셋째로, 현재 주로 연구되고 있는 양자점의 주 원료는 카드뮴으로 이에 따라 환경 유해성에 대한 논란 역시 지속되어 왔으며 카드뮴계열의

양자점을 대체하기 위한 비(非) 카드뮴 소재 양자점에 대한 연구 역시 지속되어 왔다. CdSe 양자점을 대체하기 위한 대표적인 양자점은 InP 양자점으로 CdSe 와 동일하게 핵 크기 조절을 통하여 가시광 전영역에서 빛을 발할 수 있는 에너지 밴드갭을 가지고 있다. 하지만 CdSe 양자점과 에너지 준위 차이 때문에 효율적인 전하 주입에 어려움이 있어 소자의 안정성과 효율 면에서 고무적인 성과를 보여주지 못하고 있었다. 본 논문에서는 InP 양자점의 소재 구조 개선과 더불어 InP 양자점 발광 다이오드의 소자 구조 개선을 통해 소자 성능을 획기적으로 향상시켰다. 소재에 있어서는 핵과 가까운 부위에는 Se 가 풍부하고 핵과 멀어질수록 S 가 풍부한 ZnSeS 껍질을 가지는 InP@ZnSeS 양자점을 개발하여 양자효율을 70-80 %수준으로 증가시켰으며, 소자 구조에 있어서는 InP 양자점으로의 전자 주입 장벽을 줄이기 위하여 고분자 전해질 PFN 을 삽입하여 진공 준위를 변화시켰다. 그 결과 3.46 %의 외부양자효율과 최대휘도 3900 cd/m^2 를 가지는 세계 최고 수준의 비(非) 카드뮴 양자점 발광 다이오드를 구현하였다.

본 논문은 역구조 양자점 발광 다이오드의 효율과 전하 주입을 효율적으로 증가시키기 위한 새로운 접근방법을 제시하였다. 더욱이 양자점의 물리적 특성은 소자 특성의 최대화 시키는 방법을 알아내기 위해 체계적으로 연구가 되었다. 또한 새로운 InP 양자점 발광다이오드 구조는 박막태양전지, 발광다이오드, 트랜지스터 등 다양한 광전자 소자에 적용될 수 있다.

주요어: 양자점, 발광다이오드, 역구조, 에너지 트랜스퍼, Cadmium Free, 공액고분자 전해질

학번: 2010-20799